Commissioning of Upgrades to T6 to Study Giant Planet Entry

Joseph Steer*, Peter Collen†, Alex Glenn‡, Christopher Hambidge§, Luke J Doherty¶ and Matthew McGilvray‖
Oxford Thermofluids Institute, University of Oxford, Oxford, OX2 0ES, UK

Tamara Sopek**
University of Southern Queensland, Toowoomba, Queensland, 4350, Australia

Stefan Loehle††
High Enthalpy Flow Diagnostics Group (HEFDiG), Institute of Space Systems (IRS), Stuttgart, 70569, Germany

Louis Walpot‡‡
ESA/ESTEC, Keplerlaan Noordwijk, 2201, Netherlands

The scientific potential of a mission to the Ice Giants is well recognised and has been identified by NASA and ESA as a high priority on several occasions, most recently in the 2023 - 2032 Decadal Survey. The payload capacity of such a spacecraft is limited by the heat shield thickness, which must be sized conservatively due to a lack of reliable data for convective and radiative heat flux along the proposed entry trajectories. Major upgrades to the Oxford T6 Stalker Tunnel have been commissioned that allow study of Giant Planet entry trajectories including a flammable gas handling system, a Mach 10 expansion nozzle, and a steel shock tube with optical access. Initial testing has been completed in shock tube and expansion tunnel modes with peak shock speeds of 18.9 km/s achieved. Convective heat flux and surface pressure were measured at several locations on a 45 °sphere cone model in expansion tunnel mode. Measurements of the radiating shock layer were made in shock tube mode to assess the affect of CH_4 concentration. This work establishes the first high enthalpy Giant Planet entry test bed in Europe.

Nomenclature

α = Thermal diffusivity, $m^2\,s^{-1}$

d = Non-Boltzmann local escape factor approximation

Presented as papers 2023-1339 and 2023-1729 at the AIAA SciTech Forum, National Harbor, MD, 23-27 January 2023

*DPhil Candidate, Oxford Thermofluids Insitute, University of Oxford. Corresponding author. joseph.steer@eng.ox.ac.uk.
†Postdoctoral Research Assistant, Oxford Thermofluids Insitute, University of Oxford
‡DPhil Candidate, Oxford Thermofluids Insitute, University of Oxford
§Hypersonics Operation Manager, Oxford Thermofluids Insitute, University of Oxford
¶Departmental Lecturer, Oxford Thermofluids Insitute, University of Oxford, AIAA Member
‖Associate Professor, Oxford Thermofluids Insitute, University of Oxford, AIAA Member.
**Vice-Chancellor's Postdoctoral Research Fellow For Women In STEMM, University of Southern Queensland, AIAA Member
††Head of High Enthalpy Flow Diagnostics Group (HEFDiG), Institute of Space System, Stuttgart, AIAA Senior Member
‡‡On behalf of ESA.

Γ = Damköhler number

H = Enthalpy, $\mathrm{MJ\,kg^{-1}}$

k = Thermal conductivity, $\mathrm{W\,m^{-1}\,K}$

K = Gas constant, $\sqrt{\mathrm{kg}}/\mathrm{m}$

ρ = density, $\mathrm{kg\,m^{-3}}$

ϕ = length scale, m

q = Convective heat flux, $\mathrm{MW\,m^{-2}}$

r_N, = Vehicle nose radius, mm

T_T = Translational temperature, K

T_R = Rotational temperature, K

T_V = Vibrational temperature, K

T_e = Electronic temperature, K

U = Velocity, $\mathrm{m\,s^{-1}}$

w_1 = Full width half maximum of Gaussian distribution, Å

w_2 = Full width half maximum of Lorentzian distribution, Å

Subscripts

∞ = Freestream condition

f = Thermochemically frozen condition

t = Total condition

I. Introduction

Despite the better part of a century of research attention and steady advancement, many aspects of hypersonic flow phenomena remain poorly understood. Realisation of the promise of commercial hypersonic travel, exploration of our solar system, and the establishment of humanity as a space faring species requires a continued effort to push back the frontiers of our knowledge. The gold standard of experimental data remains flight testing, however the associated costs limit their relevance to selected flight trajectories and experiments. This is particularly true in the case of planetary exploration missions, where billions of dollars of investment rely on the performance of components that cannot be flight tested a-priori. This risk is typically mitigated through a combination of advanced numerical simulations and experiments in ground test facilities. Such experiments have been demonstrated to provide useful data for vehicle development, computation model validation and insight into fundamental physics of high-speed flows.

Entries into the atmospheres of Venus, Earth, Mars, Jupiter, Saturn, Titan, Uranus, and Neptune are presently of interest to the hypersonics and planetary exploration communities. Planetary entry flows are an interplay between many

aerothermodynamic and chemical processes including convective heating, radiative heating, and material response. This complexity is difficult to replicate in its entirety in a single ground test facility, which has led to the development of specialised facilities to study different aspects of the problem separately. These include, broadly, continuous facilities such as plasma wind tunnels [2, 3] and inductively-coupled plasma torches [4], and impulse facilities such as shock tubes [5], expansion tunnels [6], and reflected shock tunnels [7]. One important aspect relevant to Gas Giant entry is that the entry profiles require that vehicles pass through high altitudes at high speeds, resulting in the formation of large non-equilibrium shock layers for much of the flight [8]. To obtain similarity between flight and experiment in a ground test facility for flows that feature significant regions of non-equilbrium thermochemistry necessitates matching the Damköhler number, defined as:

$$\Gamma = \frac{\rho_\infty \phi}{U} \tag{1}$$

where ρ_∞ is the freestream density, ϕ is an appropriate length scale, and U is the freestream velocity [9]. Matching the Damköhler number ensures that the rate of binary reactions is the same between the two flows. However, if other engineering properties such as convective and radiative heat flux are of interest, it is also necessary to match the flow total enthalpy. Stalker [10] calculated that a facility capable of continuous operation at re-entry conditions would require gigawatts of power to operate, meaning that impulse facilities become the most practical option for ground testing where total enthalpy matching is required. Further, Gas Giant entries are among the trajectories with the highest total enthalpy requirements, restricting the available options to the shock tube and expansion tube/tunnel.

Shock tubes are ubiquitous in fundamental fluid dynamics research because of their simplicity and versatility and are currently the best source of measurements of shock layer radiation. The reader is directed to Section II.A.1 for a detailed description of the working principle of a shock tube. A shock tube experiment aims to match gas composition, density, and shock speed, thereby obtaining direct similarity between the flight stagnation line and the shock tube flow ($\phi = 1$). Shock tube flows are considered 'chemically clean' meaning that the test gas is chemically undisturbed before the experiment takes place. This offers a significant advantage over other experimental facilities and makes shock tubes highly informative for the investigation of the chemical kinetics, non-Boltzmann behaviour, and the extent of the non-equilibrium region. Shock tubes operate most often in units of pressure, so for convenience conditions are represented in the form of density equivalent pressure as in Figure 1, where the shock tube fill pressure is selected to match the flight density of interest and hence account for the difference in temperature between the lab and flight.

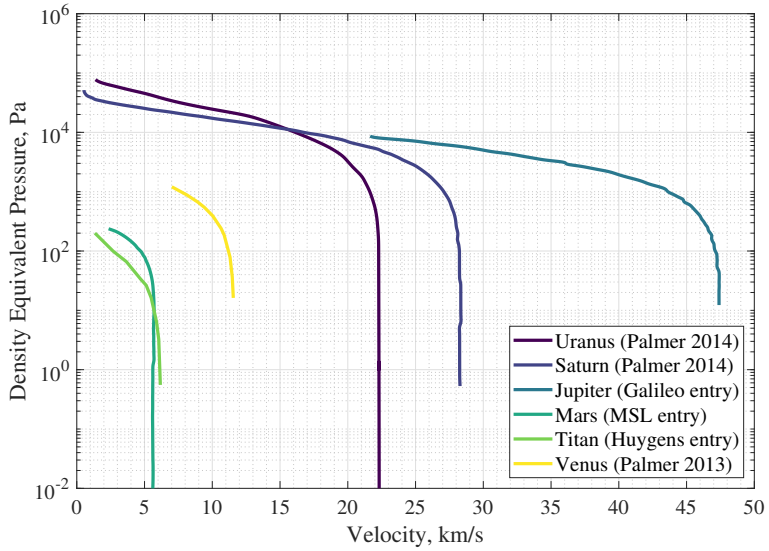

Fig. 1 Selected planetary entry trajectories presented in terms of shock tube relevant scaling parameters.

Where information about a particular flight geometry is required, expansion tunnels are more appropriate. Expansion tunnels are suited to the modelling of convective heating as they are the only facility capable of establishing thermochemically 'clean' steady flow over a sub-scale vehicle at true flight total enthalpies. The reader is directed to Section II.A.2 for a detailed description of the working principle of an expansion tunnel. The high free stream speed requirements of Ice Giant entry trajectories (18 - 23 km s^{-1}) further limit the choice of experimental facilities, leaving the expansion tunnel as the only option to model convective heat flux. In an expansion tunnel sub-scale models are used which necessitates that test conditions are binary scaled [9, 11]. Binary scaling is a method that allows the flight shock layer to be duplicated in a wind tunnel in the vicinity of the shock layer. In a binary scaled experiment, the total enthalpy (essentially $\frac{U^2}{2}$) and the post bow shock ρ_ϕ are matched to flight. This scaling replicates most of the desired properties from flight in the nose region, apart from radiation which does not scale directly. Trajectories in Figure 2 have been calculated assuming a flight length scale of 1 m. The use of different length scales means that radiation is not matched directly to flight in the expansion tunnel, however they may still be used for fundamental study of high temperature gas dynamics.

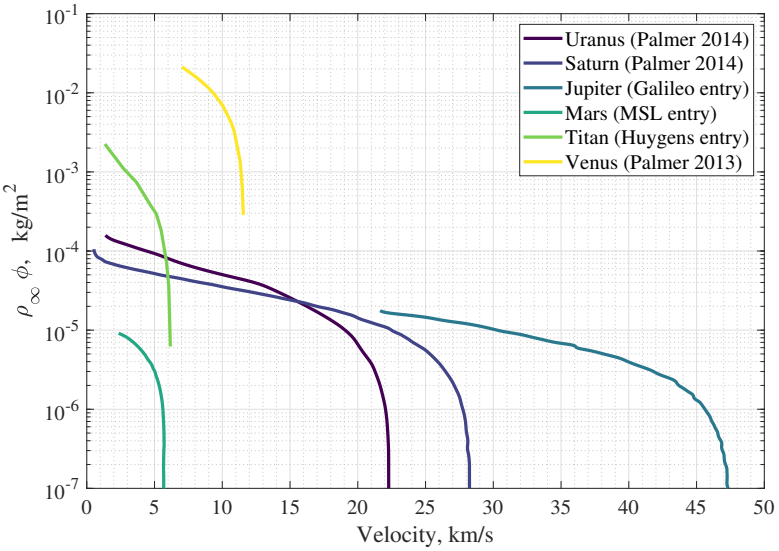

Fig. 2 Selected planetary entry trajectories presented in terms of expansion tube/tunnel relevant scaling parameters. Here, (ϕ = 1)m

Matching of the freestream velocity and gas composition is necessary for both shock tube and expansion tunnel testing and these are particularly restrictive requirements for Giant Planet entry study. As shown in Figures 1 and 2, Giant Planet trajectories are very high enthalpy which requires a large energy input to replicate. Handling the potentially hazardous H_2-He test gas mixtures necessitates the use of dedicated safety infrastructure. These requirements are stringent enough that only two pulse facilities in the world are currently operational in these trajectory ranges, the Electric Arc Shock Tube (EAST) facility at NASA Ames and the X2 facility at the University of Queensland [12].

The majority of shock radiation data for H_2-He mixtures has been obtained at NASA EAST. Initial H_2-He testing in EAST was conducted in support of the Galileo probe mission to Jupiter where shock waves travelling at up to 47 km s^{-1} were produced in 1 torr of H_2 [13, 14]. This work enabled Leibowitz and Kuo [15] to develop an analytical tool to predict electron concentrations and temperature distributions over a vehicle surface. Further experiments were run at EAST by Hollis et al. [16] to support a proposed Neptune Aerocapture mission at speeds below 30 km s^{-1}. Presently, the most complete shock tube dataset for H_2-He mixtures is that of Cruden and Bogdanoff [5].

The use of expansion tunnels to experimentally simulate Gas Giant entry was explored by Higgins [17], James et al. [6], and Liu et al. [18] at the X2 facility at the University of Queensland. These efforts make use of test gas substitution or Stalker substitution, first proposed by Stalker [7, 19]. The substitution is a method for achieving an aerothermodynamically similar environment to Gas Giant entry with less energy addition than would otherwise be required. The test gas, roughly 89 %/11 % H_2/He for Gas Giant entry, is modified with a higher percentage of He or Ne. Less energy addition is required to reach a given post-shock temperature since addition of the diluent decreases the specific heat of the gas. It was found that the substitution allowed the H_2 dissociation and ionization processes

for Uranus and Saturn entry shock layers to be simulated in X2. Although the technique is useful for modelling H thermochemistry, it is unclear what effect the substitution has on other parameters of interest, particularly heat flux.

With only two facilities currently operational and over a small range of conditions, there is a need for additional facilities to be brought online to expand the testing envelope, enable cross-facility validation studies, and provide additional testing capacity. The Oxford T6 Stalker Tunnel has a number of characteristics that make it particularly well suited to extend Gas Giant entry research undertaken at EAST and X2. Firstly, its design is multi-modal, meaning that it is capable of operating both as a shock tube (EAST) and as an expansion tunnel (X2). This endows many practical advantages but the principle scientific benefit is that a direct comparison between two types of hypersonic pulse tunnel types is possible in one place. Secondly, in comparison with EAST, T6 uses a free-piston driver, thereby avoiding issues with pre-heating effects that have been found to be significant for arc heated drivers [20]. Although later shown by Cruden and Bogdanoff [5] to not be present in later EAST data for H_2/He mixtures, it is well-accepted that a second facility with different driver technology is key for ensuring the confidence of mission designers in experimental data. Thirdly, the T6 driver is capable of producing higher burst pressures and temperatures than that of X2 and thus theoretically capable of generating higher enthalpy test conditions. James et al. [6] achieved a flight equivalent velocity of between 21.1 and 22.9 $\mathrm{km\,s^{-1}}$ in X2, sufficient for most proposed Ice Giant entries (see Figure 2), but acknowledged that reproduction of the proposed 26.9 $\mathrm{km\,s^{-1}}$ Saturn entry trajectory would not be possible. The current maximum T6 primary diaphragm rupture pressure is 29% greater than that of X2, which should translate into a higher total enthalpy capability for a given test gas density according to equilibrium predictions [21] and ultimately allow Saturn and low altitude Jupiter entry simulation.

In the present work, an overview of the T6 Stalker Facility is presented with relevant modes of operation detailed. Secondly, design upgrades to enable Gas Giant entry testing in T6 are presented with summaries of important features. Next, results from commissioning and testing with this equipment are detailed and compared to numerical predictions.

II. Facility Overview

T6 is a multi-mode hypersonic wind tunnel. A complete overview of T6 can be found in Collen et al. [1]. The free-piston driver, which generates pressures on the order of 50 MPa during a shot, may be coupled to a range of downstream components to allow operation of the facility as either a shock tube (ST), expansion tube or expansion tunnel (ExT), or reflected shock tunnel (RST). T6 offers the only expansion tube capability in Europe with test times between 20 and 150 µs.

During an experiment, a piston weighing either 36 or 90 kg is accelerated to speeds of approximately 300 $\mathrm{m\,s^{-1}}$ by high pressure air known as the reservoir gas. The gas in the volume between the piston head and the primary diaphragm, typically low pressure helium, is polytropically compressed to the diaphragm rupture condition by the piston motion. In the present work 2 x 0.4 mm score depth stainless steel diaphragms are used with a rupture pressure of 46.2 MPa and

temperature of 5000 K, corresponding to a compression ratio of 60:1 for a 35 kPa initial driver fill pressure. This high pressure, high temperature driver gas unsteadily expands into driven tube 1 (shown in Figures 3 and 5), forming the shock wave that is studied at the end of the facility.

Static pressure in the driven tubes is measured by between 9 and 17 PCB113 piezoelectric pressure transducers depending on the mode of operation. Shock speed is inferred by measuring the difference in arrival time between the transducers.

Before the potential of T6 for Gas Giant entry simulation could be realised, several major engineering upgrades were required. Firstly, T6 must be modified such that it can operate safely and accurately with H_2 mixtures. The required quantities of test gas are small (approximately 1 g) and therefore susceptible to contamination from air leakage into the system. This problem is exacerbated by the large difference in molar mass ratio between air and H_2, 1 Pa of air is equivalent to approximately 14 Pa of H_2 in terms of the number of molecules and therefore even a small leak can invalidate a test. Secondly, Gas Giant entry conditions are at the upper limit of performance of impulse facilities, requiring modification to T6 to realise the highest possible shock speed and enthalpy. These modifications took the form of upgrades to both shock tube mode and expansion tube mode. The shock speed is dependent on the condition of the driving gas, which is in turn governed by the Mach-area relation at the driver/driven tube interface presented in Equation 2.

$$\left(\frac{A_{driven}}{A_*}\right)^2 = \frac{1}{M_4^2}\left[\frac{2}{\gamma_D+1}\left(1+\frac{\gamma_D-1}{2}M_4^2\right)\right]^{\frac{\gamma_D+1}{\gamma_D-1}} \tag{2}$$

For a given orifice cross sectional area (A_*), decreasing the driven tube area increases the throat Mach number (M_4) which in turn increases the shock speed. For shock tube mode, presently, the only available tube with optical access has a diameter of 225 mm which limits the shock speed performance, a smaller diameter tube with a window to allow optical access to the flow is required to achieve Ice Giant relevant conditions.

Expansion tube mode was turned into a tunnel by the development of a Mach 10 expansion nozzle which enables an increased freestream velocity for some test conditions and have the added benefit of increasing the usable core flow area, which will permit larger length scale models to be used.

A. T6 Operating Mode Descriptions

The leading dimensions of T6 for steel shock tube mode and expansion tube/tunnel mode are listed in 1 with schematics and associated x-t diagrams presented in Figures 3 to 5. Dimensions and discussion of the capability of T6 in reflected shock tunnel mode and aluminium shock tube mode are presented elsewhere [1].

Table 1 Leading dimensions of the T6 Stalker tunnel

Section	Length m	Internal diameter mm	Outlet diameter mm
Reservoir	2.8	342.9	300.0
Compression Tube	6.0	300.0	76.2†
Shock Tube 1	2.8	96.3	96.3
Expansion Tube/Tunnel	6.0*	96.3	235.8*
Steel Shock Tube	6.0	96.3	96.3

† Orifice diameter may be altered
* Dependent on nozzle installed

1. Shock Tube Mode

T6 in SST (steel shock tube, distinct from aluminium shock tube) mode consists of a 9 m length, 96.3 mm internal diameter barrel connected to the driver and feeding in to the dump tank, as shown in Figure 3. The shock tube section features 17 axial locations where instrumentation may be installed, some of which are replicated on the opposite side of the tube (see Figure 7). The primary purpose of SST mode is to facilitate study of shock layer radiation at very high velocities. This is achieved by imaging the post-shock region through a set of 190 x 10 mm windows in the tube wall. SST mode is the highest performance shock tube configuration available on T6 because of the comparatively small internal diameter.

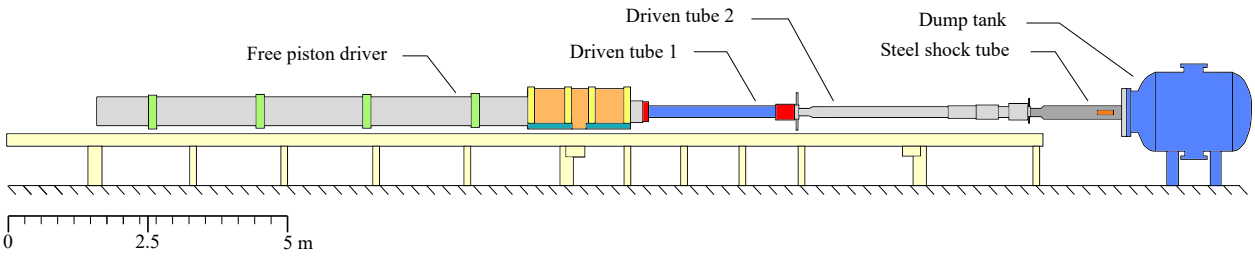

Fig. 3 Schematic of T6 in shock tube mode

Figure 4 shows a distance-time plot of the typical wave processes occurring in the tube during a test. Initially, the test gas (matching the density and composition of the flight condition of interest) resides in the region denoted 'Driven Tube 2'. The piston motion leads to rupture of the primary diaphragm and in turn drives a strong shock wave through the test gas. To obtain similarity with flight, the shock speed should match the flight case. The region of useful test gas, denoted τ, grows until it reaches a maximum value governed by the boundary layer growth [22]. The maximum achievable shock speed can be increased via the use a secondary driver [23] - this is utilised in the present work. A secondary diaphragm, in this case mylar of 10 µm thickness, is installed between driven tube 1 and driven tube 2. Driven tube 1 is then filled with low pressure helium ($\approx$ 1kPa) and driven tube 2 with the test gas. By carefully selecting the secondary driver gas fill condition it can be arranged that the shock processed secondary driver gas has a higher temperature and sound speed than could have been achieved in the expanded driver gas and therefore a stronger shock is driven through

the test gas. Use of this technique increased the maximum shock speed in this work by approximately 4 km s^{-1}.

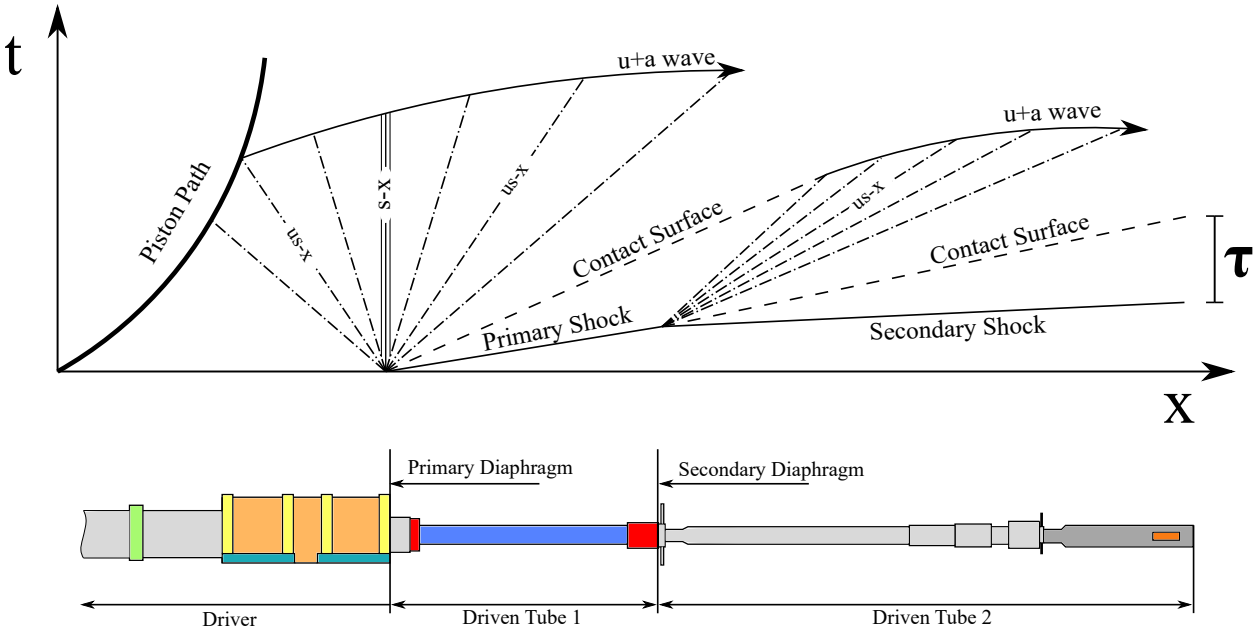

Fig. 4 Position-time diagram of wave processes in T6 shock tube mode, adapted from [1]

2. Expansion Tube/Tunnel Mode

T6 is shown in expansion tunnel (ExT mode) in Figure 5. The windowed shock tube is removed and replaced with an expansion nozzle and test section to allow study of sub-scale models. The working section, from the primary diaphragm to nozzle exit, is again 9 m long with 9 axial locations for instrumentation. The nozzle features an internal contour and expands the flow through an area ratio of 6 to the exit condition. More details about the expansion nozzle design are included in Section III.C.

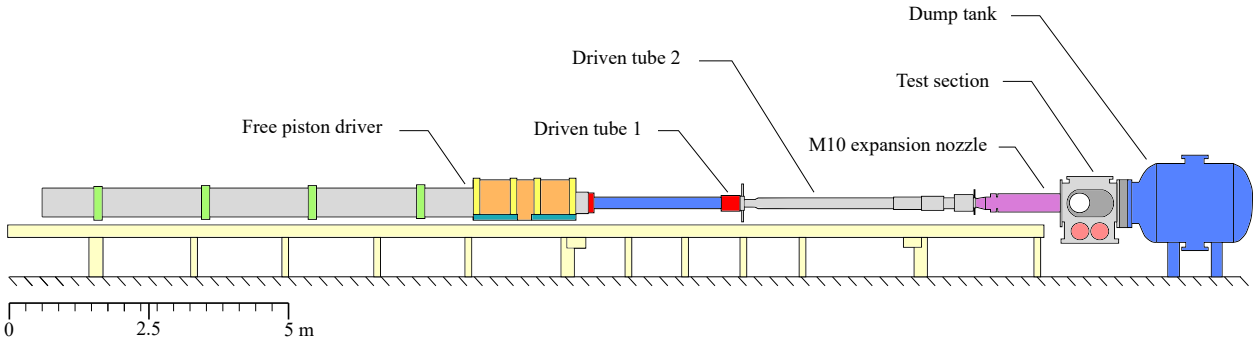

Fig. 5 Schematic of T6 in expansion tunnel mode

Figure 5 shows a distance-time plot of the wave processes occuring during an expansion tunnel test. The test gas is initially located in the region denoted 'Driven Tube 1' in Figure 5. The remainder of the working section, a volume comprised of the regions denoted 'Driven Tube 2', 'M10 expansion nozzle', 'Test section', and 'Dump tank' in Figure

5, initially contains very low density gas, typically lab air. The shock is generated in exactly the same fashion as the shock tube case, however when the shock reaches the secondary diaphragm it ruptures, allowing the high-pressure, shock heated test gas to unsteadily expand into the acceleration tube, resulting in an increase in total enthalpy without dissociation of the test gas. The expansion tube may be coupled with an expansion nozzle at the acceleration tube outlet to further expand the test gas - this arrangement is known as an expansion *tunnel*. The nozzle steadily expands the gas further and produces the final region of useful test time, denoted τ. Although other expansion tunnel facilities have operated with a secondary driver, such as X2, T6 ExT mode was not operated with one for the present work.

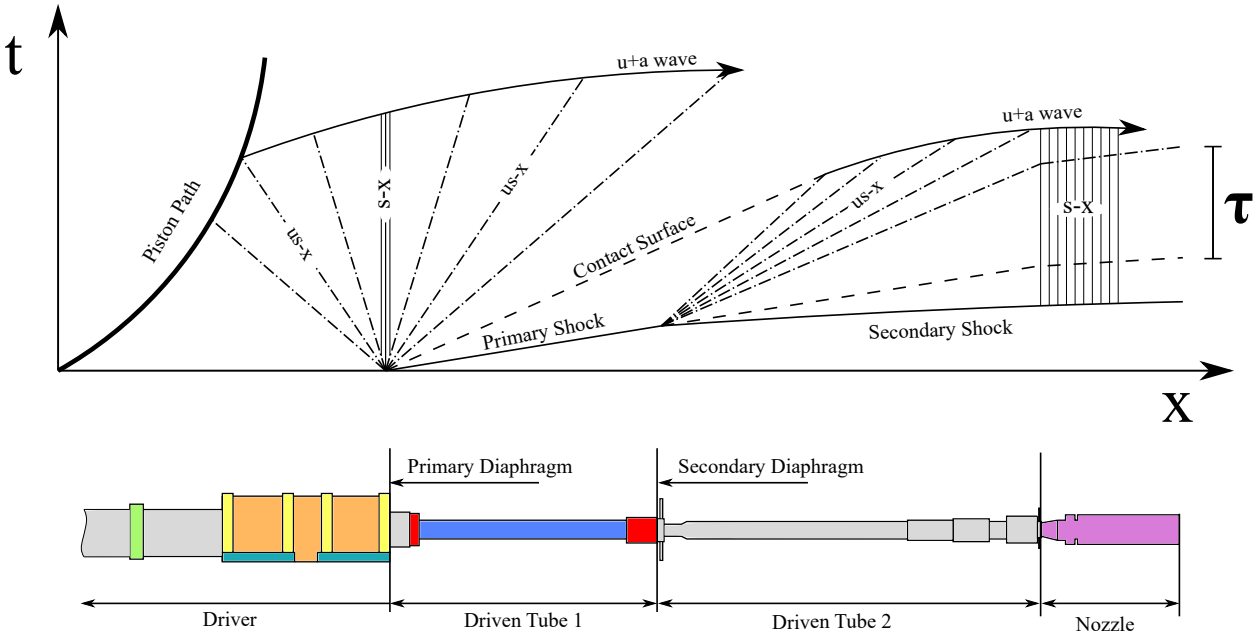

Fig. 6 Position-time diagram of wave processes in T6 expansion tunnel mode, adapted from [1]

Prior to the work described herein, T6 was not equipped with an expansion nozzle and therefore the achievable total enthalpy, core flow diameter, and maximum model size was limited. This work extends that capabilities of T6 to include operation with flammable test gases and with an expansion nozzle.

III. Upgraded Infrastructure

To enable T6 to perform Gas Giant entry research three key upgrades to the facility were required:

1) Addition of a flammable test gas handling system
2) Development of an expansion nozzle
3) Development of a new, smaller diameter shock tube with optical access

Each of these upgrades and results from their commissioning are presented and discussed in this section.

A. Flammable Test Gas

Prior to this work T6 was not able to be operated with a flammable test gas, being restricted for safety considerations to inherently inert test gases such as N_2, air or Mars atmospheric mixtures [24, 25]. The capability to use hydrogen based test gases is a requirement to simulate Gas Giant entry trajectories, regardless of the mode of operation. Although only 0.025 g of H_2 is required for a single test, the system was sized for a maximum of 1 g of H_2, thereby future proofing operation of the flammable gas system for use in other studies.

Physical upgrades to the facility include:

- An N_2 purge system that was sized to ensure the maximum quantity of H_2 could be diluted to less than 1% concentration by volume, or less than 25% of the lower flammability limit
- Modifications to the logic of the facility Programmable Logic Controller (PLC) to ensure operators undertake appropriate evacuation and purging cycles prior to introducing H_2 to the facility
- A test gas fill cylinder to facilitate rapid precise filling of the shock tube at very low fill pressures
- A dedicated vent system to allow disposal or pure H_2 to the atmosphere in the event of an emergency
- A flammable gas detection system in the laboratory area

One challenge with operating shock tubes for shock layer radiation experiments, and particularly for Gas Giant entry conditions, is ensuring an accurate fill pressure and composition prior to arrival of the incident shock. As a part of the upgrades the filling process was altered to improve accuracy. As part of the new system, a sample cylinder of variable volume (300 - 5000 cc) was evacuated and pressurised to 1 - 3 bar with the test gas while isolated from the driven tubes. Prior to the test, the contents of the sample cylinder were introduced to the evacuated driven tubes and allowed to equalize in pressure via a nearly ideal process ($p_1V_1 = p_2V_2$) where the test pressure is measured on a low range gauge. There were two sample cylinders installed, one for each driven tube, allowing for precise filling of the acceleration tube or secondary driver as well as the test gas.

Hydrogen embrittlement of metallic components in the system was a consideration during the design process. The study of the specific mechanisms of hydrogen gas embrittlement of metals is an active area of research which is summarised by Michler et al. [26]. The typical experimental procedure for quantifying the effect of hydrogen embrittlement is to apply a constant strain rate to a tensile specimen in a high pressure hydrogen environment. The extent of embrittlement is determined by examining the relative reduction in cross sectional area of the specimen at failure versus a control case at standard atmospheric conditions. Although hydrogen embrittlement is strongly material dependent phenomenon, it is generally observed to worsen as temperature and pressure increase. For the grades of carbon steel employed in the construction of the T6 system, the effect of hydrogen embrittlement was judged to be negligible because of the low operating pressures and temperatures [27, 28].

The new test gas filling system allows filling of each driven tube with flammable gas to final pressures of between 1 Pa and 10 kPa with an accuracy of ±0.1%.

B. Steel Shock Tube

A new steel shock tube featuring two 190 x 10 mm windows was designed to facilitate study of the shock layer at Ice Giant entry conditions via spectroscopy. A section view of the new barrel is shown in Figure 7. The tube has successfully been fitted to the existing infrastructure and passed hydraulic testing at 175 bar. The final assembly is 2055 mm in length and weighs approximately 750 kg. The tube incorporates eight axial locations to mount shock timing stations, which at five locations feature holes on both sides of the tube. The tube also features a tertiary diaphragm station so that the driven tube volume can be isolated from the dump tank volume, allowing higher vacuums to be achieved and minimising the quantity of hydrogen required to reach a given test pressure. A large port just downstream of the measurement windows allows connection to a turbo-molecular pump with minimal pumping resistance. With this arrangement an ultimate vacuum of less than 1 mPa was achieved with a leak rate of less than 1 mPa s^{-1}.

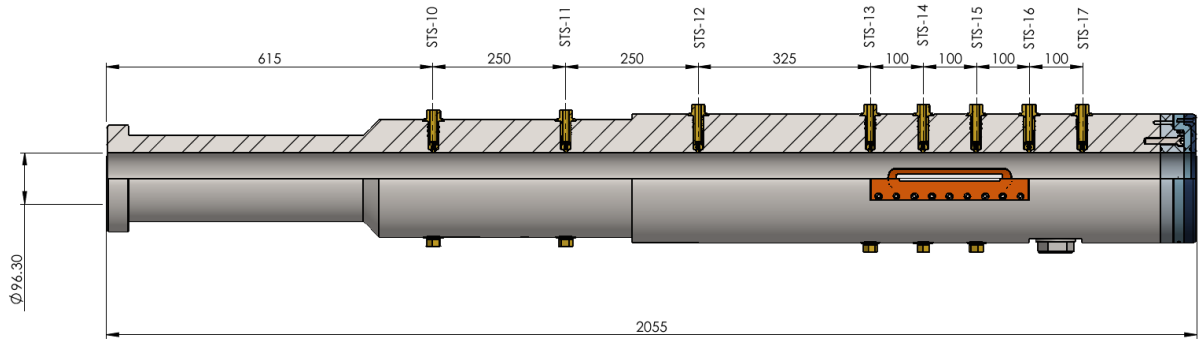

Fig. 7 Schematic of the new T6 steel shock tube

C. Expansion Nozzle

The classical converging-diverging (or de Laval) nozzle exploits the Venturi effect by choking the flow to produce high velocity and in turn high thrust at the outlet. Nozzles of this type are used widely in hypersonics research, for example in reflected shock tunnels where the test gas is stagnated at the nozzle throat before being expanded to the test condition [29]. In the case of a shock tube or expansion tube, the test gas is already in a supersonic/hypersonic state before it reaches the nozzle and hence no converging section is required to choke or stagnate the flow. Nozzles of this type are known simply as expansion nozzles. Trimpi and Callis [30] were the first to investigate the benefits of coupling an expansion nozzle to an expansion tube and showed that, from a purely theoretical point of view, the apparatus would offer increased testing time, larger initial test-gas slug length, higher efficiency, and reduced secondary-diaphragm bursting problems. Callis Jr [31] continued their work at Langley and considered the effect of placing the nozzle before the secondary diaphragm in order to mitigate disturbances from the opening process. This configuration was ultimately rejected due to the high driver pressures required to achieve an equivalent performance to the now conventional

placement of the nozzle after the secondary diaphragm.

Scott [32] designed and built a 1.4 m contoured expansion nozzle for the X2 facility at the University of Queensland using a Nelder-Mead optimization algorithm. The nozzle was optimised to produce a Mach 10 flow with the largest possible core flow diameter. Although there were some differences between the predicted and experimentally observed exit properties the test flow was found to be doubled in length and of high enough quality to facilitate model testing. Following the success of this work, Davey and Litster [33] simply scaled up the contour of this nozzle for use on the larger X3 facility after CFD validation in Eilmer 3. Based on the findings of the CFD analysis, Davey elected to truncate the length of the scaled nozzle by 0.5 m as it was observed to have negligible effect on the outflow properties. Whereas the X2 nozzle had been manufactured from mild steel, the new X3 nozzle was manufactured by fibre wrapping composite around a wooden mandrel. This change in technique was required to limit the weight of the nozzle which would have been in excess of 500 kg had mild steel been used. The work of Davey has essentially been replicated for the design of the T6 expansion nozzle.

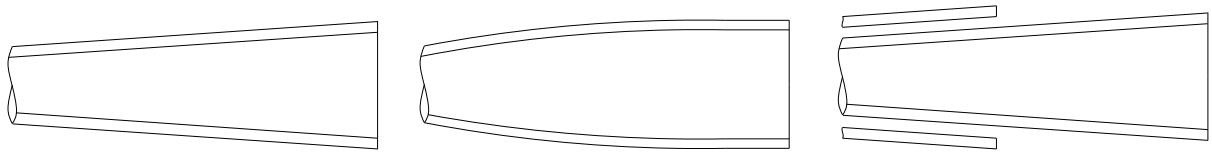

(a) Conical nozzle **(b) Contoured nozzle** **(c) Skimmer nozzle**

Fig. 8 Common nozzle geometries

More recently, Toniato et al. [34] used a parallel simplex algorithm to design an optimised Mach 12 expansion nozzle for the purpose of testing a REST scramjet engine in the X3 expansion tunnel. Experimental testing of the nozzle revealed that a Mach number of 11.1 ± 0.9 with a test time of 1.3 ms was achieved. The discrepancy to the target Mach number was due to an excessively thick boundary layer in the acceleration tube, which could only be addressed by shortening the X3 acceleration tube.

To accelerate the design and manufacturing process the nozzle contour was scaled from the X2 expansion nozzle contour, originally designed by Scott [32]. The same process was followed by Davey and Litster [33] to design the X3 expansion nozzle contour which proved successful in terms of the achieved test time and core flow. The nozzle was not truncated as was done by Davey and Litster [33] as the final required overall length was not prohibitive. The original profile optimised using the method of characteristics and was defined in terms of 10 Bezier control points. A straight section was included before the beginning of the nozzle profile.

The nozzle was designed and static tested to an internal pressure of 75 bar, corresponding to the expected pressure encountered during passage of the driver gas after a test. Considerations were also given to the axial loading encountered by the nozzle during facility recoil after a shot via inclusion of a design safety factor, however the magnitude of this loading is not well established. Although the nozzle functions as a vent during a test it was designed and tested as a

static pressure vessel.

The nozzle was designed to a working pressure of 50 bar and hydraulically pressure tested to 75 bar. This working pressure was chosen as it corresponds to the driver gas pressure and drove the external geometry and wall thickness design of the nozzle. Figure 9 presents a CAD rendering of the final design. To facilitate precise machining of the internal contour it was machined in two pieces from 7075-T6 aluminium and features four cardinal mounting points for sensors at the outlet.

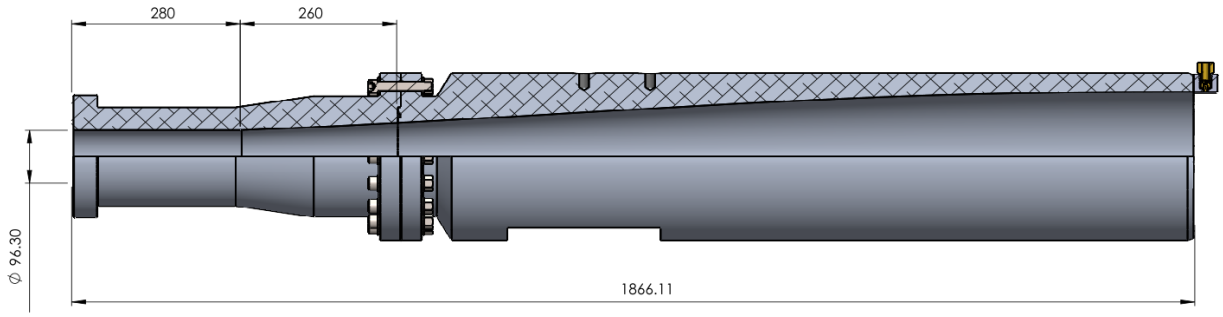

Fig. 9 Section view of the new Mach 10 expansion nozzle

D. Summary of upgrades

The upgrades presented in this section represent major changes to the T6 architecture that must be tested experimentally to verify their usefulness. The remainder of this document concerns the initial test series with the new equipment, firstly in shock tube mode and secondly in expansion tunnel mode.

IV. Shock Tube Mode Results

Results from the commissioning of new shock tube mode infrastructure are presented here. The primary objective of these experiments was to measure the radiating shock layer at the maximum performance level in shock tube mode. Although significant progress in Gas Giant entry research has been made in the last ten years, many studies have neglected the influence of trace components such as CH_4 on the aeroheating environment. In a review paper, Moses et al. [35] summarise the observed abundance of tropospheric and stratospheric constituents on the Ice Giants. These values are reproduced in Table 2.

Recent simulations from Coelho [36] indicate that the presence of 1.5% CH_4 will have a significant effect on the radiative heating environment for entry speeds as low as 18 km/s where previously it was thought that no significant radiation would be present until 25 km/s or greater. The bulk of the deceleration and therefore aeroheating for Ice Giant trajectories is expected to occur in the stratosphere [12], where CH_4 abundance on Neptune is expected to be an order of magnitude lower than the value modelled by Coelho - abundance on Uranus is expected to be three orders of magnitude

Table 2 Stratospheric composition of the Ice Giants by volume from [35]

Species	Uranus	Neptune
CH_4	16 ppm at 50 mbar	0.115% at 5 mbar
C_2H_2	0.25 ppm at 0.2 mbar	0.033 ppm at 0.5 mbar
C_2H_4	$<2 \times 10^{-14}$ at 10 mbar	0.8 ppb at 0.2 mbar
C_2H_6	0.13 ppm at 0.2 mbar	0.85 ppm at 0.3 mbar
C_3H_4	0.36 ppb at 0.4 mbar	0.12 ppb at 0.1 mbar
C_4H_2	0.13 ppb at 0.4 mbar	0.003 ppb at 0.1 mbar
CO_2	0.08 ppb at 0.14 mbar	0.78 ppm at 0.1 mbar
CO	6 ppb at 0.5 mbar	1.1 ppm at 0.1 mbar
H_2O	3.8 ppb at 0.03 mbar	2.5 ppm at 0.16 mbar
D/H	4.4×10^{-5}	4.1×10^{-5}

lower. Given that the Decadal Survey has identified a Uranus mission as the priority the requirement for detailed studies of surface heat flux with CH_4 mixtures is lessened. However, establishing this capability will still be informative for modelling of the atmosphere and heat shield recession post-flight.

A. Performance map

Conditions for nominal composition (85 % H_2 / 15 % He) and methane-doped (0.5% and 5% CH_4) gas mixtures have been developed and are detailed in Table 3. In order to achieve the high shock speeds required for Ice Giant entry, a pure helium secondary driver was utilised in all tests. The secondary driver and test gas fill pressures, psd_1 and p_1 respectively, were selected in order to maximise the achievable shock speed. The primary and secondary shock speeds, U_{s1} and $U_{s2/\infty}$ respectively, were calculated using measurements from shock timing stations distributed along the length of the facility.

Table 3 Summary of conditions tested in shock tube mode

Condition	Symbol	Test Gas Composition, %v/v	psd_1, Pa	p_1, Pa	U_{s1}, km/s	U_{s2}, km/s	Slug Length, mm	Slug Time, µs
A	●	85 % H_2 / 15 % He	1000	12.9	8.8	16.7	38	2.3
B	■	84.5 % H_2 / 15 % He / 0.5 % CH_4	1000	12.8	8.8	16.4	39	2.4
C	◆	80 % H_2 / 15 % He / 5 % CH_4	1000	13.0	8.8	16.3	41	2.5

Figure 10 shows the measured shock speeds for each condition. Moderate shock deceleration was observed in most tests. For example, the shock speed in shot 372 (spectra not reported in the present work) peaked at 18.4 $km\,s^{-1}$ but decelerated to 17.0 $km\,s^{-1}$ by the time it reached the observation window. Shock speed uncertainties were calculated using the method detailed by James [37] and as such are much higher near the observation window due to the decreased

sensor spacing. The peak shock speed seen in the campaign was 18.9 km s^{-1} in T6s365 for condition B where the fill pressure was 0.1 torr.

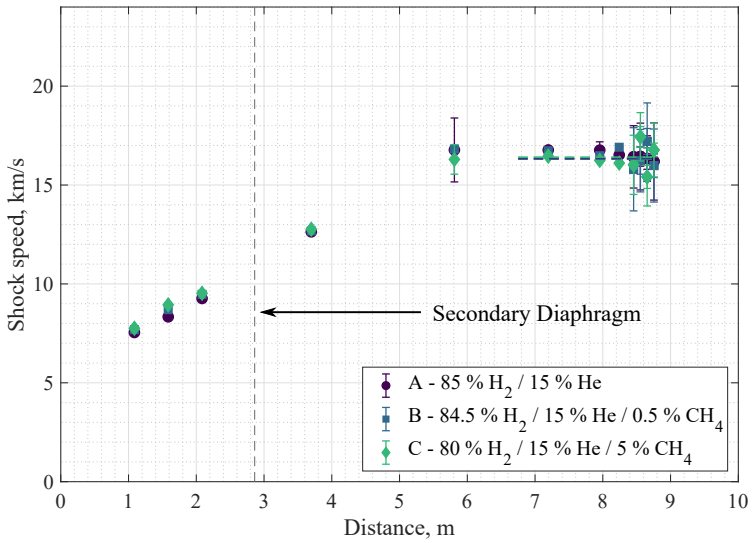

Fig. 10 Shock speed profiles for tested conditions

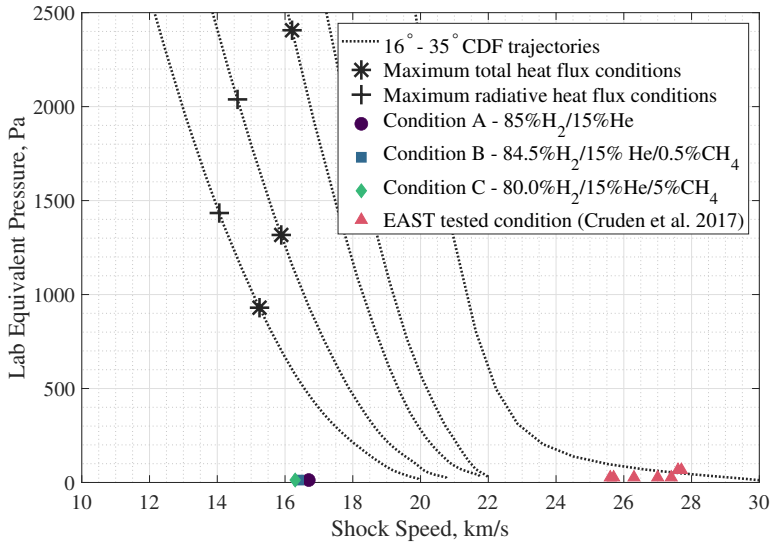

Fig. 11 Plot of achieved performance in shock tube mode

Figure 11 shows a comparison of the achieved experimental performance versus several candidate Ice Giant entry trajectories proposed by ESA [12]. Similarity between facility and flight is obtained along the stagnation line when freestream velocity and density are matched. For a given pressure, the temperature in the lab is typically higher than what would be encountered in flight and therefore the atmospheric density is converted to an equivalent pressure at

laboratory conditions, which is what is shown in Figure 11. Fully theoretical PITOT [21] predictions for the existing 'high' driver condition of 46.2 MPa, a secondary driver fill of 1 kPa pure helium, and test gas fill pressures of 0.1, 1.0, and 10.0 torr are also included. PITOT is a state-to-state code which assumes thermochemical equilibrium in all processes.

T6 was able to match the peak heating shock speeds for several of the trajectories in this preliminary test series which is a first for a European shock tube facility. Although the equivalent pressure could not also be replicated, many options for improving the facility performance are available include reducing the diaphragm opening time which would necessitate a different diaphragm material. Design of a more powerful driver condition is also possible as well as utilising pure H_2 as a secondary driver gas. H_2 has a higher speed of sound than He for an equivalent pressure and temperature, thus allowing a stronger shock to be driven through the test gas. The test gas substitution technique proposed by Stalker and Edwards [19] could also be explored to expand the operating envelope as has been done at X2.

Figures 12 and 13 show the static pressures at the observation window and the Pitot pressures at the tube outlet respectively. The data have been shifted such that shock arrival corresponds to 0 µs. The test slug occupies only the first 2 µs by considering the Mirels slug length and experimental shock speeds. This makes it difficult to reliably discern the pressure during the test time since the response time of the pressure transducers used is 1 µs. CEA predicts post-shock pressures of 3.1, 3.3, and 4.1 kPa for conditions A, B, and C respectively if the average shock speed over the last five shock timing stations is used as the input. However, since the pressure across the contact surface is equal an accurate judgement of the test slug pressure can be obtained from the experimental traces in Figure 12 which are in good agreement with CEA predictions.

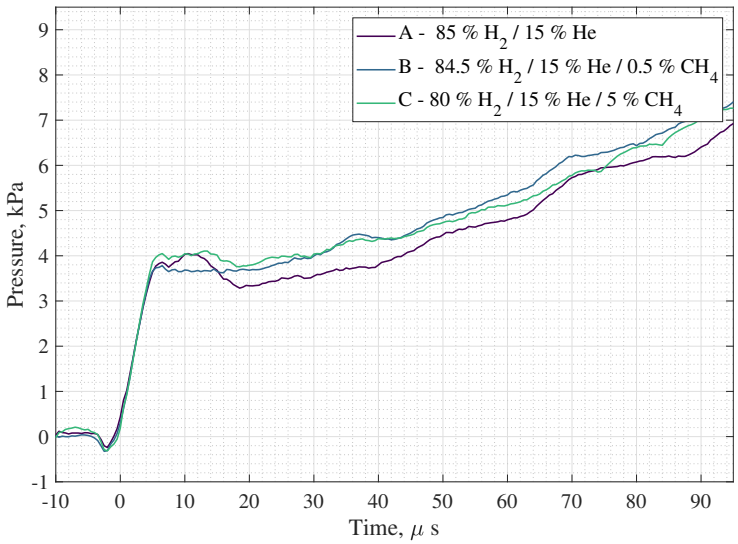

Fig. 12 Static pressure

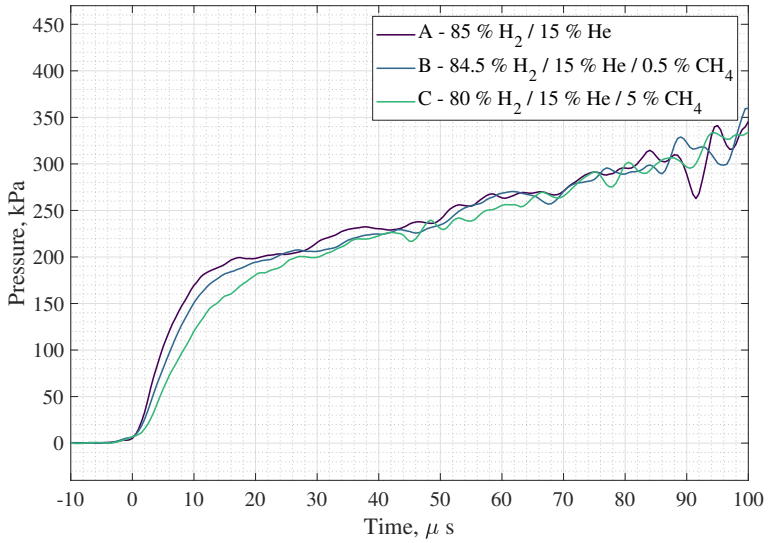

Fig. 13 Pitot pressure

B. Optical Emission Spectroscopy

Although the conditions obtained in the preliminary test series are below those proposed by ESA for an Ice Giant entry mission, the spectra obtained still provide a valuable insight into the non-equilibrium thermochemistry taking place in the test slug and by extension in the flight shock layer. Emissions from the radiating shock layer were recorded via a PI Isoplane-320 Spectrograph coupled to an Andor iStar-sCMOS. The measurement window used was UV grade fused silica from Crystran Ltd, a black coloured blank was installed on the opposite side of the tunnel to minimise the impact of reflections on the data. Before each test a spatial, intensity, and wavelength calibration of optical setup were performed. Spatial calibration of the spectrometer was achieved with the aid of a custom alignment plate. The plate was designed to bolt onto the opposite side of the tube and had holes drilled along the centreline of the tunnel with a positional tolerance of 0.05 mm. By lighting the back side of this plate with a diffuse light source the holes were clearly visible in the sCMOS view as near points. These points were then used as reference to set the desired field of view of the spectrometer via fine adjustment of optical mirrors. Intensity calibration of the spectrometer was achieved via the use of an integrated light source. The model used was a Bentham SRS8 Integrating Sphere. During the calibration process, the integrated light source was fixed to the opposite side of the tube and positioned in the line of sight of the spectrometer. A series of images were then collected using the 'accumulate' feature on the Andor camera, each image having the same exposure time and gain settings as the test exposure. The same process was then completed with the integrated light source off which provided a reference background image. Wavelength calibration was completed using a Princeton Instruments IntelliCal Hg and Ne/Ar arc lamp. The calibration and post-processing techniques used have been described in detail by Collen et al. [1] and Glenn et al. [38]. A schematic diagram of the experimental setup used

is shown in Figure 14.

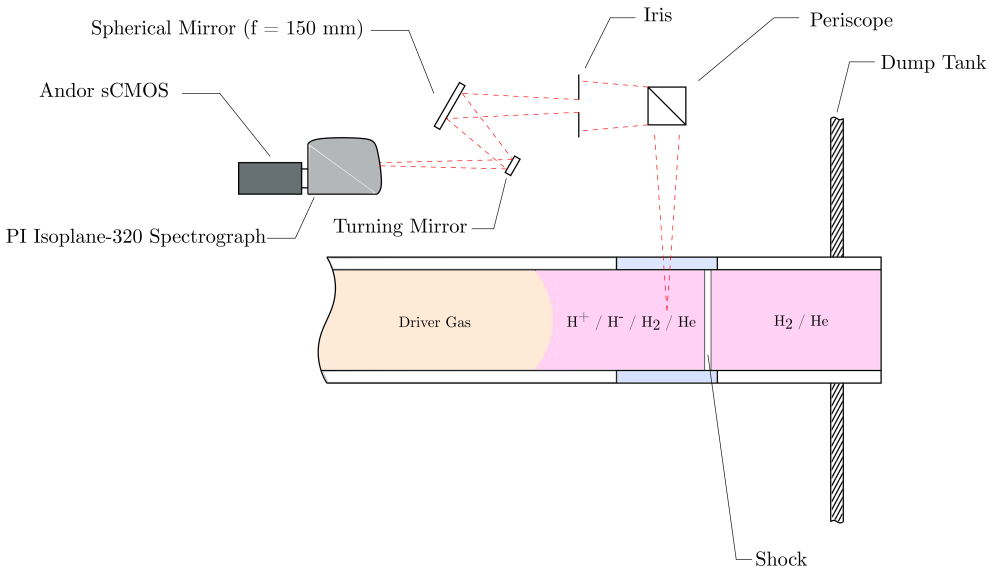

Fig. 14 Schematic diagram of the optical emission spectroscopy setup used in shock tube mode, adapted from [1]

The Andor camera was triggered using a micro-controller based delay generator. The controller monitors the pressure signals at two locations close to the end of the shock tube and then predicts the time of arrival of the shock at the window. As a compromise between signal to noise ratio and spatial resolution, a camera exposure time of 500 ns was used for initial experiments, but the gating time was later reduced to 250 ns to minimise the effect of spatial smearing. The shock moved an average of 4.1 mm during the gating time for the conditions reported in Table 3. The spectrometer was centred on the 350 - 570 nm wavelength region.

Experimental data for the conditions described in Table 3 are shown in Figures 15, 16, and 17. The data are characterised by a non-equilibrium peak and subsequent relaxation toward equilibrium. The magnitude of spectral radiance at the peak and in the immediate post-shock region appears to be strongly affected by the concentration of CH_4 in the test gas - the maximum spectral radiance at the peak increases by approximately an order of magnitude for each increase in CH_4 concentration. It is believed that equilibrium is not reached for any of the cases as the observed radiance did not reach a steady level by the end of the test slug. The lines indicate the extent of the test slug as predicted by Mirels' theory [22].

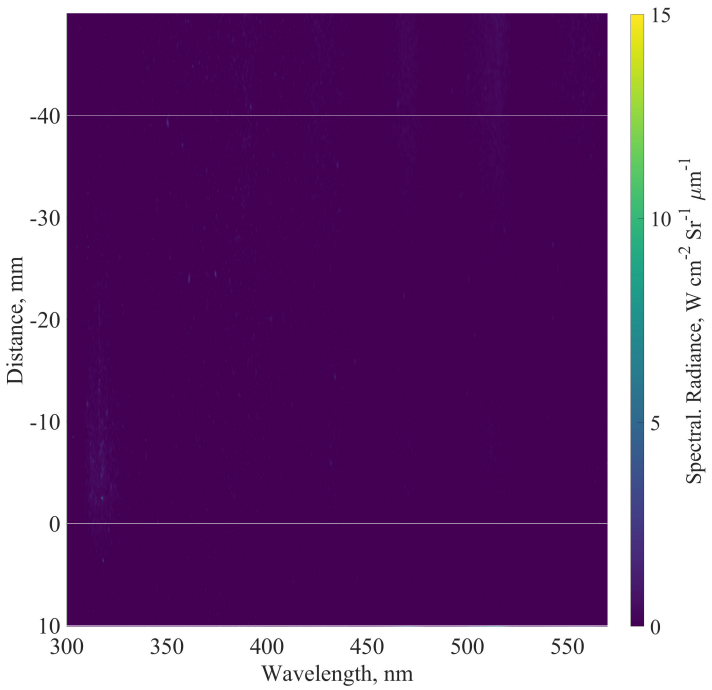

Fig. 15 0% CH_4

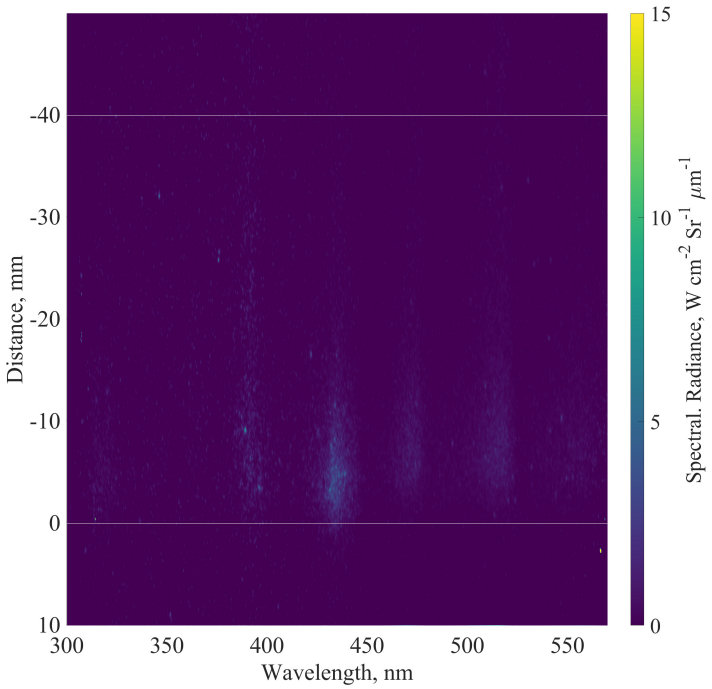

Fig. 16 0.5% CH_4

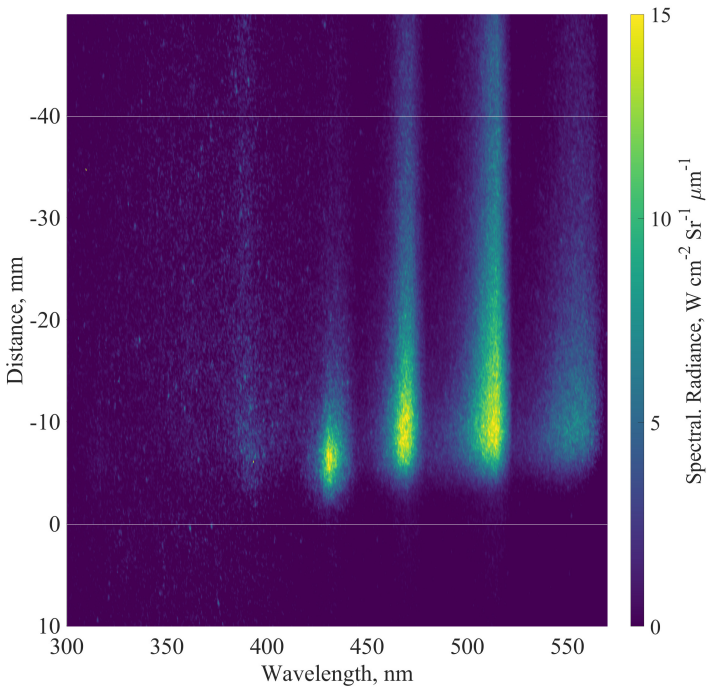

Fig. 17 5% CH_4

Figure 18 shows spatial radiance profiles for the three conditions. The profiles have been shifted so that the non-equilibrium peak corresponds to 0 mm. Again, the concentration of CH_4 strongly influences the observed post-shock radiance. The data in Figure 18 clearly demonstrate the importance of considering CH_4 in the design of entry missions to Gas Giant planets. The presence of CH_4 in a planets atmosphere may require that additional accommodations are made by mission designers to ensure that adequate heat shield margin is available. Further analysis of the observed spectra is presented in the next section.

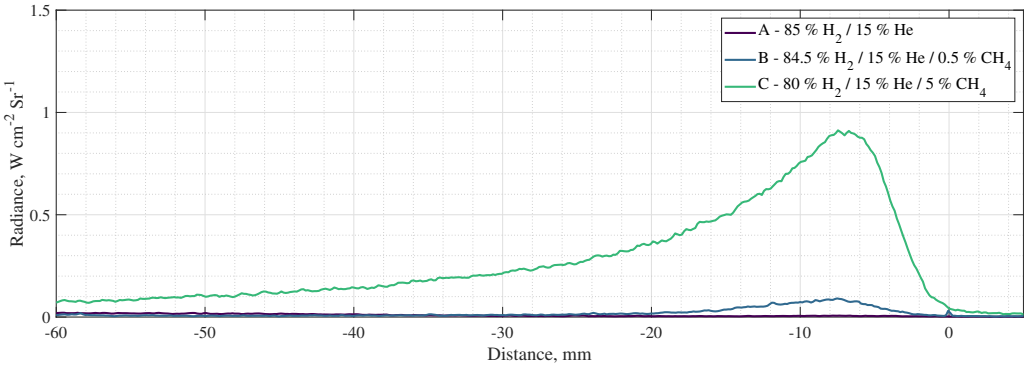

Fig. 18 Spatial radiance profiles. 0 mm indicates the non-equilibrium peak, the flow is travelling left to right i.e. negative values are further post-shock

C. NEQAIR Spectral Fitting

The Nonequilibrium Radiative Transport and Spectra Program (NEQAIR) program, first developed by Park [39], is a code for simulating radiative transport which is a benchmark for comparison to shock tube data. Version 15.0 allows the user to perform a 'spectral fit' where NEQAIR produced spectra can be tailored to match closely with experimental data. The program will run a simulation with a given set of initial conditions and then vary T_T, T_R, T_V, T_e, and species concentrations in order to improve the fit. A range of different optimisation algorithms are available, however the default *trf* (a trust region optimisation algorithm) is used in all of the present work. The full capabilities of the code are summarised by Cruden and Brandis [40]. Spectral fitting was performed for each condition to provide an indication of the thermochemical state of the gas.

In all NEQAIR simulations presented here the state population method was set to be non-Boltzmann with the full local calculation absorbtion method with a local escape factor approximation of d = 1.0. The geometry was set to be a shock tube with diameter of 96.3 mm, equal to the T6 internal diameter. Boundary conditions were set with no initial radiance and blackbody at the final LOS point temperature so that incident radiant heat flux was returned. The simulation wavelength range was set to between 410 and 570 nm which is the region where a good match to experimental data could be reliably obtained. Manual grid spacing was selected with a resolution of 4 Å. The ICCD1 scan function was selected with a scanned grid spacing of 4 Å. Full width half maxima for the Gaussian and Lorentzian contributions to the convolution function were w_1 = 24.70 and w_2 = 0.01 respectively. The scan was set to include the entire region. These values have been previously found to match the slit function of the experimental data well [38]. The LOS point used in spectral fitting was the NEQAIR default. Only C2 and CH species were included in the spectral fitting simulations as other species were not observed to contribute to the level of radiation. Further details of this analysis are available in Steer et al. [41].

1. 0% CH_4

Negligible radiance was observed for the 0% CH_4 mixture, as shown in Figure 19. The radiance levels are very close to the noise floor of the camera and thus the measurements are relatively noisy. Evidence of the Balmer series lines at 486, 434, and 410 nm is notably absent, indicating that no excitation of H_2 has occurred as might be expected in the equilibrium region. The observations are consistent with the findings of Cruden and Bogdanoff [5]. No spectral fitting was performed for this condition as the signal was deemed too weak to provide a useful result.

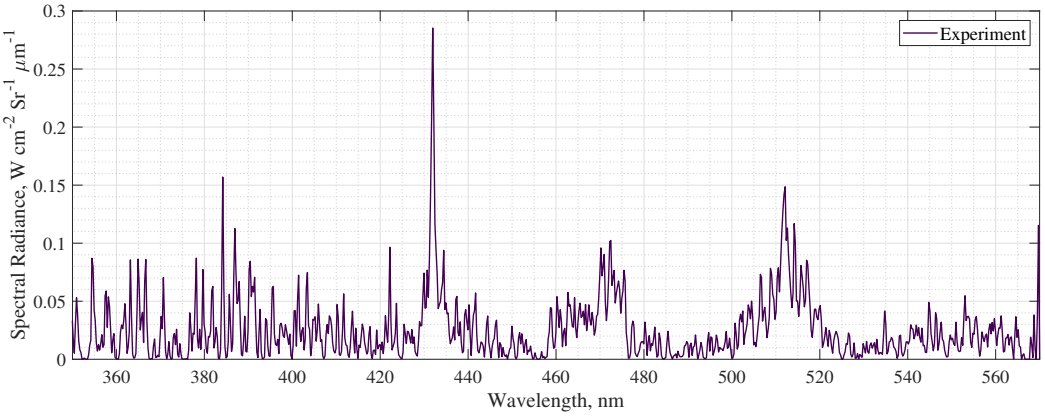

Fig. 19 Condition A non-equilibrium peak radiance

2. 0.5% CH_4

Figure 20 shows the spectral contributions of different species to the condition B non-equilibrium peak profile as predicted using the NEQAIR spectral fitting routine. Only C2 and CH were included in NEQAIR simulations as this provided the best fit with experimental data. Radiation at the peak is dominated by the CH(A-X) band centred at 430 nm. Similarly to many diatomic molecules, CH radiates strongly in the infrared region, much more so than in the visible region. IR spectroscopy may be an interesting technique to use in future studies of H_2-He-CH_4 mixtures. A large contribution is also made by the Deslandres-D'Azambuja band system of C2 which begins at approximately 430 nm and continues to the end of the experimental wavelength range (570 nm). Again, there is no clear evidence of atomic radiation. The results from a NEQAIR simulation using the predicted CEA equilibrium species number densities are shown in red.

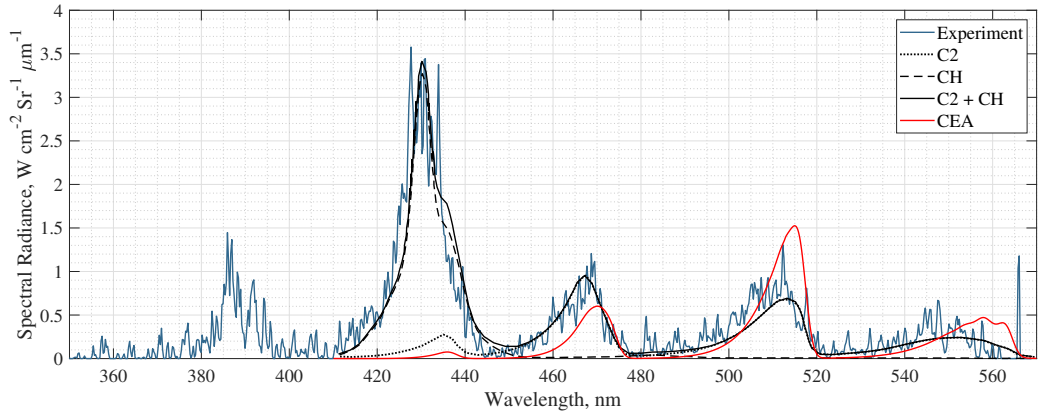

Fig. 20 Contributors to condition B non-equilibrium peak radiance

The spectral feature between 380 and 400 nm was not C2 or CH according to NEQAIR simulations. The inclusion of other species likely to be present according to a CEA run also did not yield a satisfactory reproduction of this feature.

It should be noted that many of the species predicted to be present at equilibrium by CEA and/or included in the reaction scheme of Park [42] are not implemented in NEQAIR, possibly due to a lack of radiation transition probability data in the literature. Addition of these species may lead to a better fit to experimental data.

3. 5% CH_4

The dominant radiator for the condition C non-equilibrium peak is the Deslandres-D'Azambuja band system of C2, followed by the CH(A-X) band. Interestingly, radiation from the CH(A-X) band peaks slightly before the total radiation peak. This is a demonstration that CH forms more readily than C2, possibly because of the greater availability of reactants (CH_2, C, H_2, H as reported by Park [42] vs just C). Again, there is no clear evidence of atomic radiation, however it could be that there are atomic lines present but they are insignificant when compared to the molecular radiation.

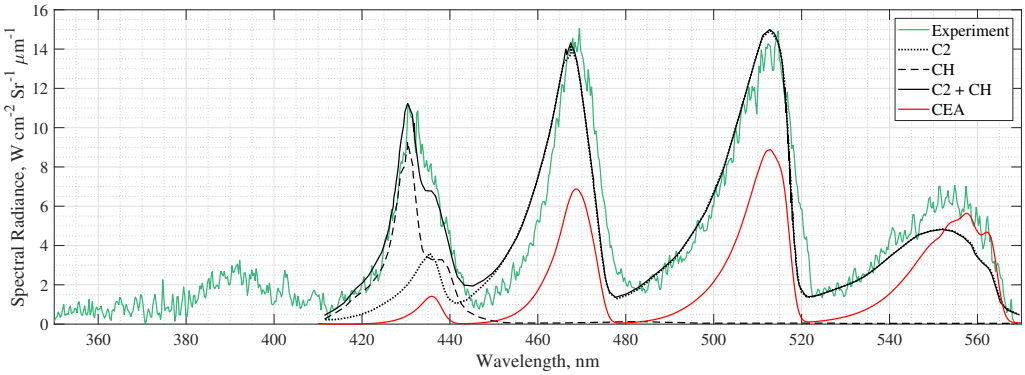

Fig. 21 Contributors to condition C non-equilibrium peak radiance

As with the 0.5% case, the feature between 380 and 400 nm was not present in NEQAIR simulations. Additionally, the band feature beginning at approximately 530 nm appears to be under predicted. Again, this could be because of the presence of species that are not currently implemented in NEQAIR.

V. Expansion Tunnel Mode Results

In this section, results from commissioning of the new expansion tunnel infrastructure are presented. This includes a performance map for the facility, a summary of the nozzle performance and core flow analysis, as well as preliminary results from scaled model testing at Ice Giant entry conditions.

A. Performance map

Conditions for nominal composition (85 % H_2 / 15 % He), Stalker substituted, and nominal composition with methane (0.5 % and 5 % CH_4) gas mixtures have been developed and are detailed in Table 4. The shock tube and acceleration tube fill pressures, p_1 and p_5 respectively, were selected in order to maximise the total enthalpy of the

test gas for condition A. The primary and secondary shock speeds, U_{s1} and U_{s2} respectively, were calculated using measurements from 9 shock timing stations distributed along the length of the facility. The freestream total enthalpy (H_0)and density (ρ_∞) have been calculated using PITOT [21].

Table 4 Summary of tested conditions. Values derived using the PITOT code assuming thermochemical equilibrium

Condition	Symbol	Test Gas Composition, %v/v	p_1, Pa	p_5, Pa	U_{s1}, km/s	$U_{s2/\infty}$, km/s	H_0, MJ/kg	ρ_∞, kg/m^3
A	●	85 % H_2 / 15 % He	2360	2.20	8.92	18.4	176	6.15e-5
B	■	40 % H_2 / 60 % He	2610	2.50	8.46	17.1	154	7.80e-4
C	◆	15 %H $_2$ / 85 % Ne	2330	2.50	7.56	14.0	105	1.06e-4
D	★	84.5 % H_2 / 15 % He / 0.5 % CH_4	2550	2.50	8.37	16.4	142	1.22e-4

Figure 22 shows the measured shock speeds for each condition. As expected, the maximum shock speed was observed for condition A where the largest fraction of H_2 is present. A secondary shock speed of 18.39 km s^{-1} (corresponding to a flight equivalent velocity of 18.90 km s^{-1}) was achieved.

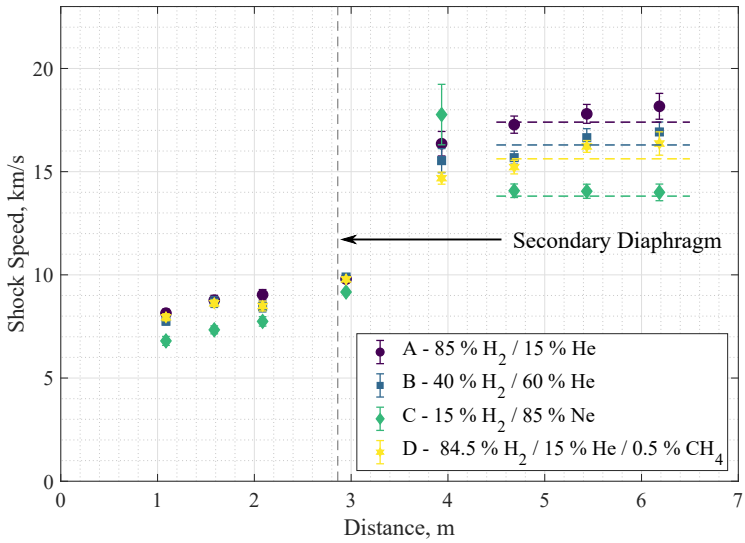

Fig. 22 Comparison of shock speeds

Figure 23 shows a comparison of the achieved experimental performance for condition A versus several candidate Ice Giant entry trajectories proposed by ESA [12]. PITOT simulations tuned to experimental performance for the existing 'high' driver condition of 46.2 MPa, a test gas fill pressure of 2.3 kPa and a range of acceleration tube fill pressure between 10.0 and 0.5 Pa are also shown as an indicator of the achievable performance. T6 is able to access many of the proposed ESA trajectories including peak heating in two cases, which is another first for a European impulse facility.

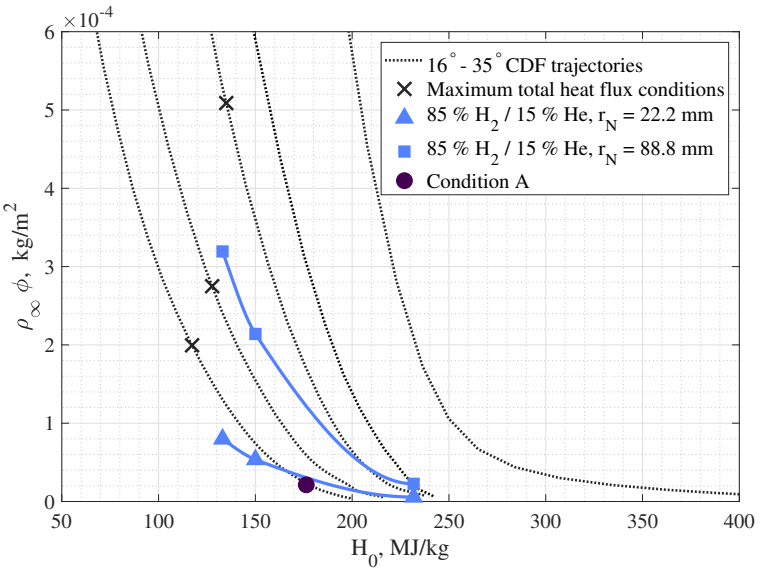

Fig. 23 Binary scaling performance map

A wide parameter space remains available to improve the facility total enthalpy performance. The acceleration tube fill pressure is strongly related to the achievable total enthalpy as shown in Figure 23. The use of thinner secondary diaphragm material could be explored to reduce losses. Additionally, a new driver condition could be designed. It is believed that losses through the primary diaphragm could be lessened by reducing the diaphragm opening time which would necessitate a different diaphragm material. Design of a more powerful driver condition is possible, but may require manufacture of a lighter piston which is not trivial. A 76.3 mm orifice was installed downstream of the primary diaphragm for these tests which could potentially be removed to offer greater performance. To simulate higher density trajectory points, an experimenter could increase the test gas fill pressure, increase the model size, run without an expansion nozzle which sacrifices core flow size, or increase the acceleration tube fill pressure which would decrease total enthalpy.

It is interesting to consider how implementing a secondary driver in T6 expansion tunnel mode, as done at the X2 facility, could further improve performance. Simulations using the Pitot tool have been run to assess the performance of utilising a pure hydrogen primary driver, secondary driver, and accelerator gas, both individually and in tandem. A loss factor calibrated against the theoretical Pitot prediction for condition A and the actual experiment is applied to both density and flight equivalent velocity predictions. The results are shown in Figure 24. These changes could allow access to direct simulation of Saturn entry conditions and also lower density Jupiter entry conditions.

B. Nozzle experimental performance

A Pitot rake was setup in the test section to record the nozzle outflow properties and thereby assess the suitability of the conditions for model testing. The rake has 11 slots spaced at regular 20 mm intervals to house type 113 PCB

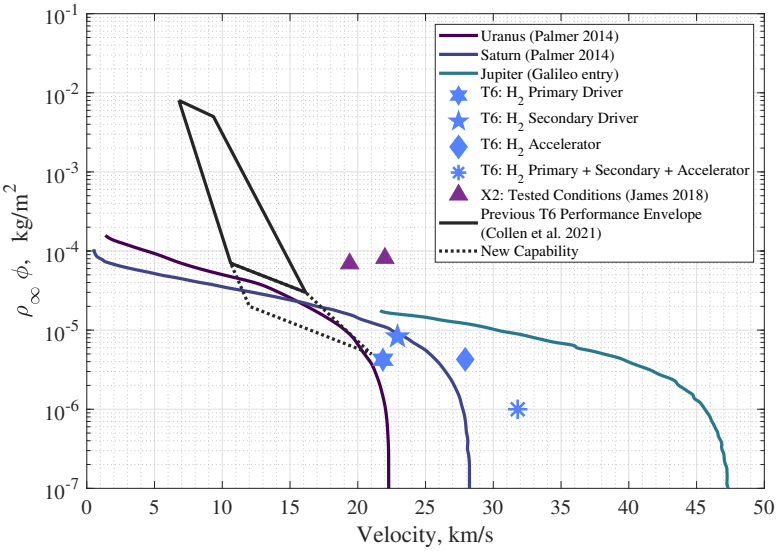

Fig. 24 Predicted T6 performance against proposed Giant Planet entry trajectories with a pure hydrogen primary driver, secondary driver, and accelerator gas.

pressure transducers. The rake was located 20 mm downstream of the nozzle outlet and on the nozzle center line. A pressure transducer was also located at the nozzle exit plane in order to measure the static outlet pressure. More detailed information about the T6 pitot rake can be found in Collen et al. [43].

Figure 25 shows pitot pressure traces obtained over the test time for condition A (Table 4). The data indicate that steady flow persists for 30 - 50 μs before the arrival of the driver gas. The negative pressure seen just before shock arrival was likely caused by electrical interference from the highly ionised accelerator gas. Figure 26 shows the test time averaged Pitot pressure for each sensor in the rake versus the radial location, 0 mm being the nozzle centerline. PP11 records a lower pressure than the others, indicating that it was outside the nozzle core flow. Considering the geometry of the rake, this gives a core flow diameter of at least 160 mm. The uncertainty associated with each point in Figure 26 is simply one standard deviation of the measurements in the test time. The results in Figures 25 and 26 demonstrate the success of the expansion nozzle design and its suitability for hypersonic testing.

CFD studies of the nozzle contour were run to reconstruct the test flow. The flow solver used was Eilmer 4 [44, 45]. The simulation was axisymmetric and time accurate. The inlet to the domain was assumed steady and uniform, with values of static pressure, velocity, and temperature set by experimental measurements and Pitot predictions (Table 4. A portion of the constant diameter acceleration tube was included to allow for boundary layer development by the beginning of the nozzle contour. The length of acceleration tube modelled was chosen to match the boundary layer thickness observed in the experimental data. The final grid was 600 x 100 nodes across the nozzle contour region. A single temperature, finite rate chemistry 85%H_2-15%He gas model was used with reaction scheme from Park [46].

A comparison between the experimental data and the final simulation for condition A is shown in Figure 26. Good

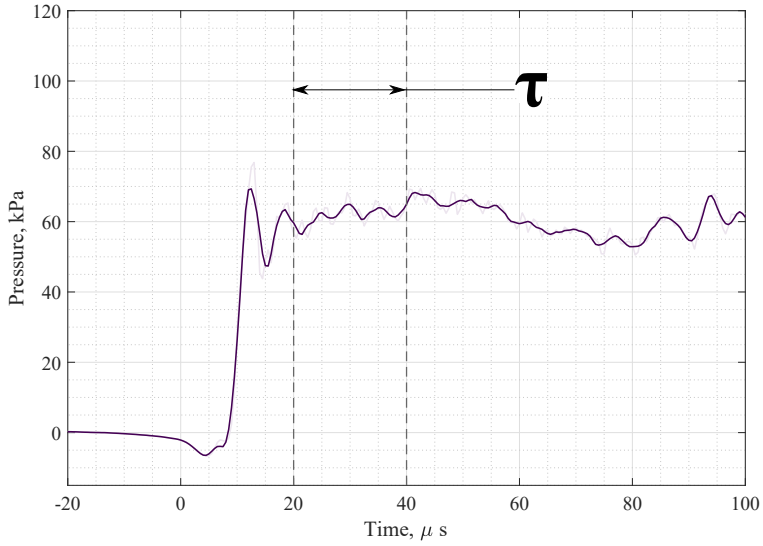

Fig. 25 Centreline Pitot pressure trace. τ indicates the test time

agreement with the experiment is seen which provides confidence in the achieved test conditions. The largest discrepancy is seen at PP11 which is not surprising since PP11 is most affected by the incoming boundary layer state. Figure 27 shows contours on Mach number and density obtained from simulations of condition A. These contours indicate that density is also uniform in the core flow which is critical to the validity of the $\rho_\infty \phi$ scaling.

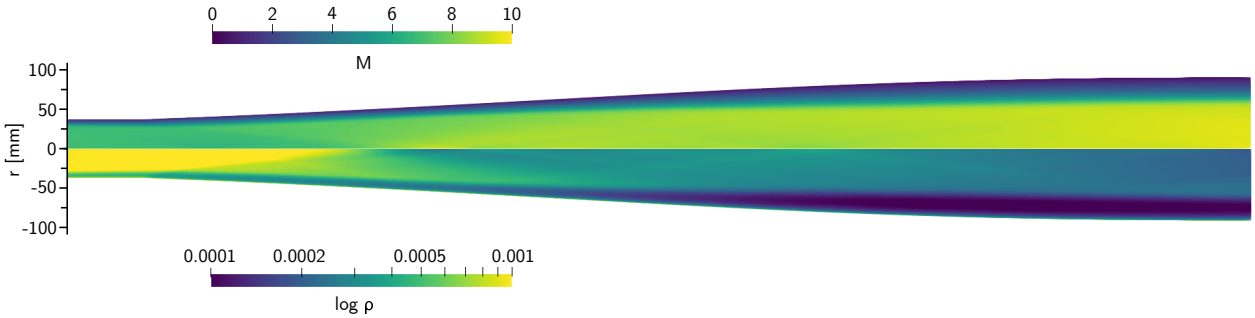

Fig. 27 Contours of Mach number and density obtained from Eilmer 4 simulations of condition A

C. Model testing

The design of the capsule model is based on dimensions of the Galileo spacecraft heat shield, a 45 °sphere-cone. The scaling of the model was determined primarily by the predicted nozzle core flow size of between 180 mm and 200 mm in diameter for Ice Giant test conditions. A planform diameter of 126 mm was selected, corresponding to a 1:10 scaling of the Galileo probe. The model had a nose radius of 22.2 mm (ϕ in the $\rho_\infty \phi$ scaling parameter). The model was machined from EN24 steel and was surface hardened to 60 HRC. To allow for mounting of the model in the T6 test section the backshell was not machined and the model was truncated at the end of the sphere-cone geometry. The model

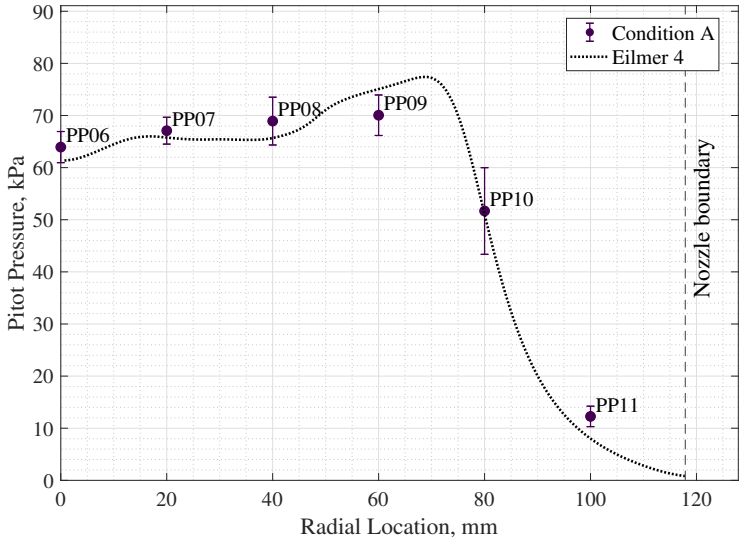

Fig. 26 Test time averaged Pitot pressures

is pictured in Figure 28.

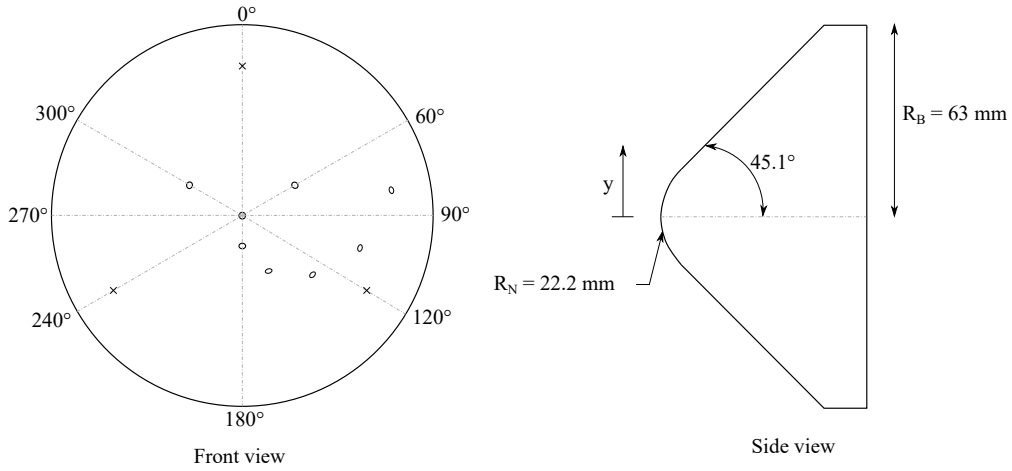

Fig. 28 Schematic diagram of the instrumentation layout for the Galileo sub-scale model. 'x' indicates a pressure transducer and 'o' indicates a coaxial thermocouple.

The model was instrumented with both thermocouples to infer heat transfer and pressure transducers to infer angle of attack. Six K-type coaxial thermocouples from the Medtherm corporation were installed flush against the model surface at 10 mm intervals starting at the stagnation point. This type of thermocouple has a response time of approximately 1 μs and has been widely used in hypersonic ground test facilities. K-type sensors were selected so that the probe material would have values of the thermal diffusivity, α, and thermal conductivity, k, that matched the corresponding wall material value of $\sqrt{\rho c k}$ (or $k/\sqrt{\alpha}$) as nearly as possible. The sensors have an outer diameter of 0.061" (1.54 mm) and a tube length of 0.25" (6.35 mm). The manufacturer quoted sensitivity and thermal product of the sensors were 41

μV (type K) and 8665 $Jm^{-2}K^{-1}s^{-0.5}$ respectively.

A total of 11 shots were completed with the sub-scale model installed. The focus of these experiments, aside for demonstrating the Ice Giant capability of T6, was to produce reliable heat transfer data and establish best practice for the use of the optics setup. All test conditions were harsh with small pits and abrasions evident on the model surface. Several thermocouples were destroyed over the course of the test campaign. Figure 29 shows a colour image obtained with the DSLR camera during the test time for condition D, which provides an indication of the observed luminosity during tests.

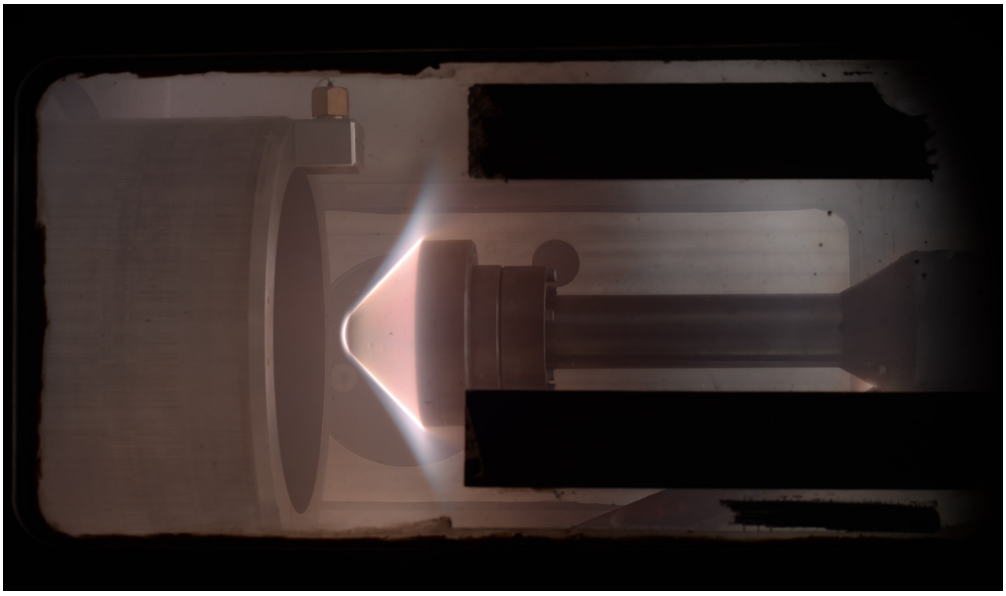

Fig. 29 Single frame colour exposure during the test time for Condition D

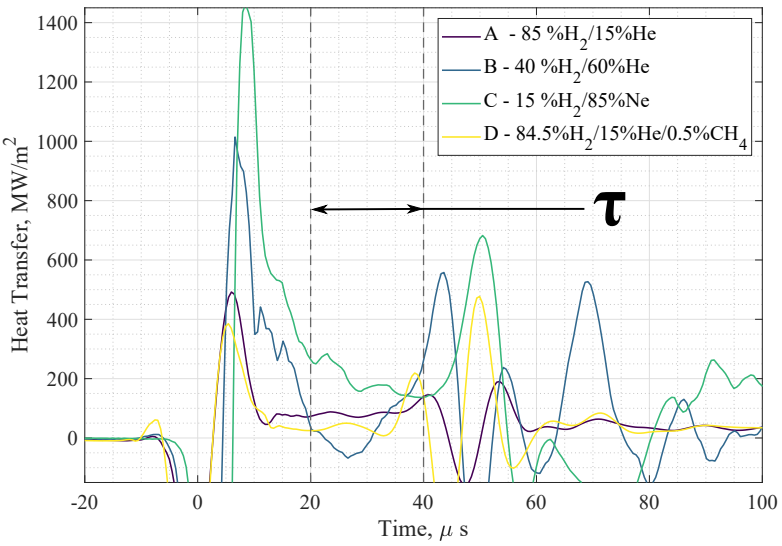

Fig. 30 Model stagnation point heat transfer. τ indicates the test time

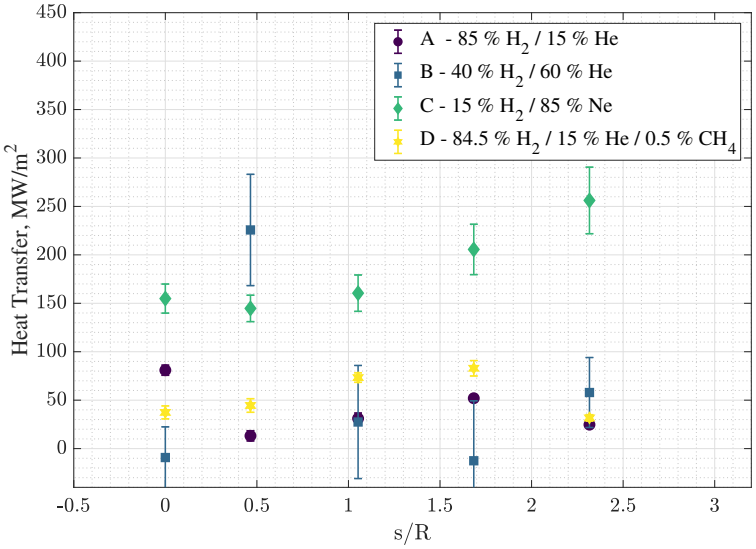

Fig. 31 Model heat transfer normalised by s/R

Figure 30 shows processed heat transfer traces at the stagnation point for each test condition, the test time begins at 10 µs. Each of the traces is characterised by a large 'dip' just before flow arrival. This feature is possibly spurious and due to the highly ionised accelerator gas creating RF interference in the thermocouple circuitry. In general, the traces for conditions B and C were much noisier than conditions A and D. This may be because the test gas in conditions B and C was more ionised and therefore electrically noisy. The heat flux for condition B dips and becomes negative during the test time which is clearly non-physical. This could because the thermocouple was struck by a diaphragm fragment or other debris.

Figure 31 shows a plot of the test time averaged heat flux against the normalised surface distance to nose radius ratio for each thermocouple. In all cases heat flux generally increases when moving away from the stagnation point. This trend is reminiscent of recession data obtained from the Galileo probe entry to Jupiter [47–49] where recession at s/R = 3.3 was 88% of the stagnation value. However, it should be noted that the Galileo shock layer environment was strongly dominated by radiation and thus is not directly comparable to these data.

Table 5 shows the average stagnation point heat flux for each condition versus the corresponding Sutton & Graves convective prediction [50]. The correlation is of the form:

$$q_{conv} = 0.487K\sqrt{\frac{\rho_\infty}{R_n}}U_\infty^3 \tag{3}$$

Where K is a gas constant, ρ_∞ is the freestream density, R_n is the sub-scale vehicle nose radius, and U_∞ is the flight equivalent velocity. Values for density were taken from Table 4 with K calculated based on the H_2 mass fraction of interest. Additional details are available in Steer et al. [51].

Table 5 Summary of test time averaged stagnation point heat flux versus Sutton and Graves prediction

Condition	K	S&G, MW/m^2	Experiment, MW/m^2	Δ, %
A	1.38e-4	22.3	78.9	254
A [§]	1.38e-4	22.3	79.5	257
B	1.88e-4	33.95	-5.3 [*]	-116
C	4.19e-4	116.0	154.9	33.5
D	1.40e-4	24.6	35.0	42.4
D [†]	1.40e-4	24.6	27.4	11.5

[§] With MgF_2 coating
[*] Measurement affected by likely diaphragm fragment impact
[†] With SiO_2 coating

Clearly, the experimental measured heat fluxes, in general, differ significantly from those predicted by Sutton. This is likely due to issues with the heat flux measurement already discussed, but it is worth noting that the correlation of Sutton is only predictive of convective heat flux, is only validated to an enthalpy of 116.2 MJ kg^{-1} (although it has been shown to be highly effective outside this range), and is being used in a form that neglects the effect of wall temperature.

The work of Carroll et al. [52] has shown that heat flux predictions from Data Parallel Line Relaxation (DPLR) CFD simulations for Ice Giant entry deviate from the predictions of Sutton and Graves Jr [50]. Alternate correlations are proposed, one for a hot wall and one for a cold wall case. The cold wall correlation is used here for comparison purposes. The correlation is a function of the stagnation point static pressure, which not directly measured. If chemical equilibrium is assumed, a value of $p_{stag,s}$ = 19.5 kPa is obtained which is used in the present calculation. The correlation of Carroll predicts a stagnation point heat flux of 32.1 MW m^{-2} for condition A, approximately 50 % more than the value predicted by Sutton. Carroll notes that the largest deviations from Sutton's predictions were found at lower densities and radii ($\rho = 1 \times 10^{-5}$ kg m^{-3} and R = 0.2 m were the smallest values considered by Carroll) so this difference is not surprising. Again, this updated correlation does not aim to include the contribution of radiation, although it is expected to be and is found to be small in the present work.

The heat flux results presented are, to the author's knowledge, the first characterisation of the Ice Giant entry convective heating environment around a representative vehicle geometry. They highlight the difficulties associated with thermocouple measurements in a high-enthalpy, highly ionised shock layer, namely the clear presence of electrical interference in some cases. Future experiments should utilise alternate measurement techniques that are protected from the ionised flow environment, such as calorimeters or infrared thermography, that can provide further context for the data presented here.

D. Optical diagnostics

A Kirana high-speed camera was set up perpendicular to the flow plane as shown in Figure 32 to record video of the test time. The frame rate was set between 1 million and 2 million FPS with an exposure time between 100 and 500 ns depending on the expected brightness of the condition. The settings allowed the time from 20 µs before flow arrival to 60 µs after to be captured which included arrival of the accelerator gas through to completion of the test time.

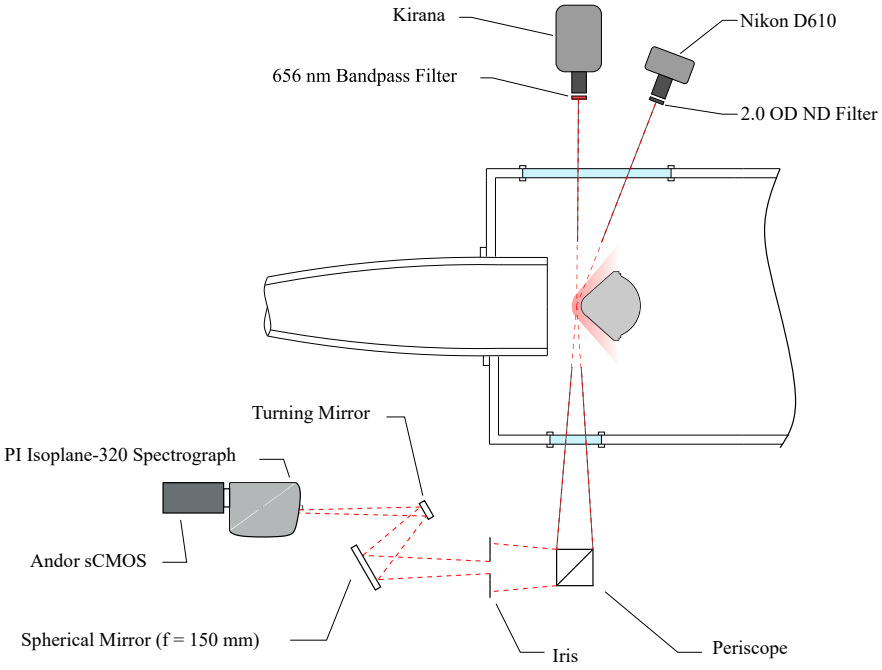

Fig. 32 Schematic diagram of the optics setup used in initial Gas Giant entry experiments

Selected frames from the high speed video obtained with the Kirana are shown in Figure 33. The images in Figure 33 are unfiltered i.e. no bandpass filter was installed. Despite the very low exposure times, the sensor saturated for every shot, however this footage was still useful for verification of accelerator and test gas arrival.

A spectrometer system was also set up for some of the tests, as shown in Figure 32. The arrangement and method of calibration is identical to that presented in Section IV.B, however here it was focused along the model stagnation line, rather than the tube centreline. Setup in this fashion allows for longer exposure times to be used, in this case 30 µs, because the shock layer is stationary in the camera's frame of reference and therefore no spatial smearing occurs.

Figure 34 shows the spectral data obtained along the vehicle stagnation line for condition A. The signal levels are low, with the H-α atomic line only faintly visible close to the vehicle surface (0 mm). This finding is generally consistent with previous work on H_2/He shock layers, most recently Liu et al. [18].

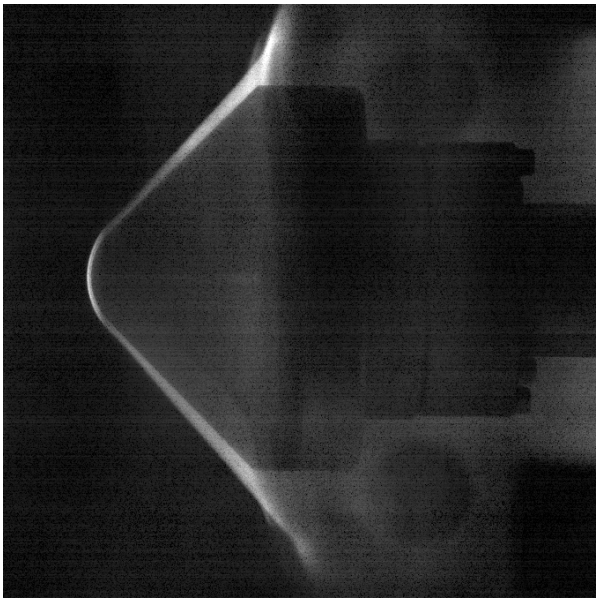

(a) Condition A

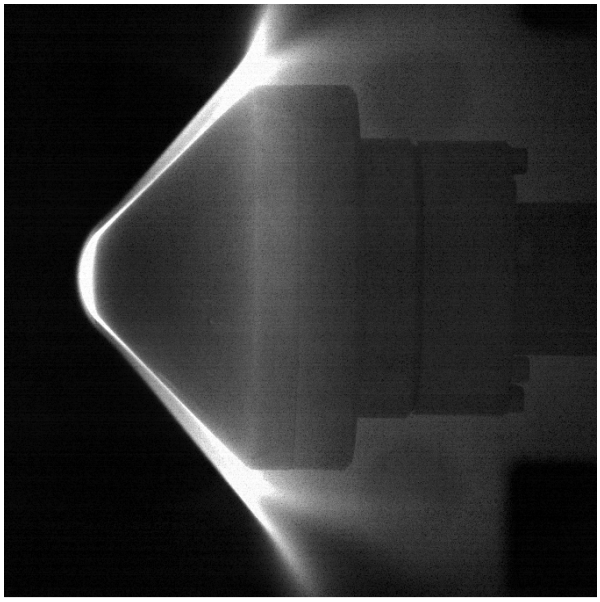

(b) Condition B

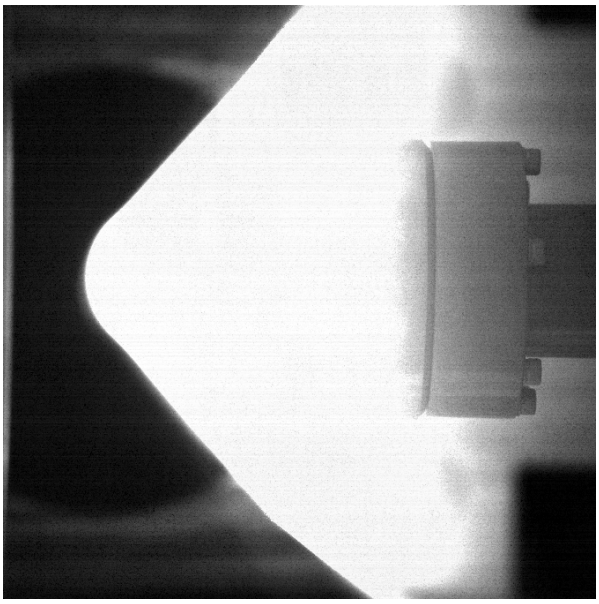

(c) Condition C

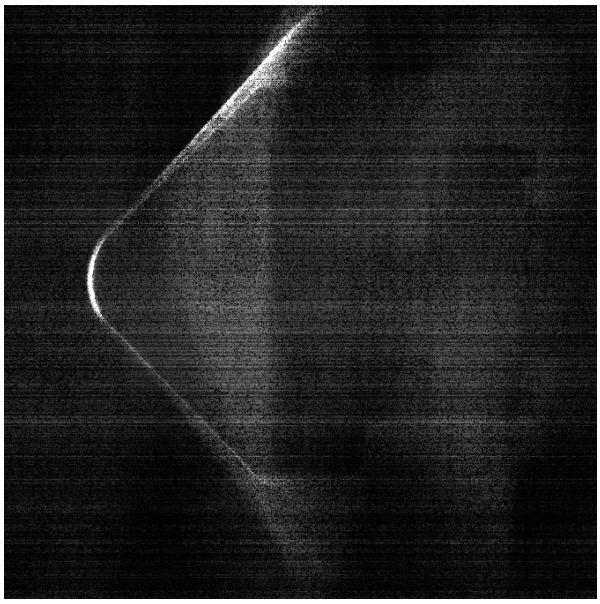

(d) Condition D

Fig. 33 Selected single frames from high speed video of the test time

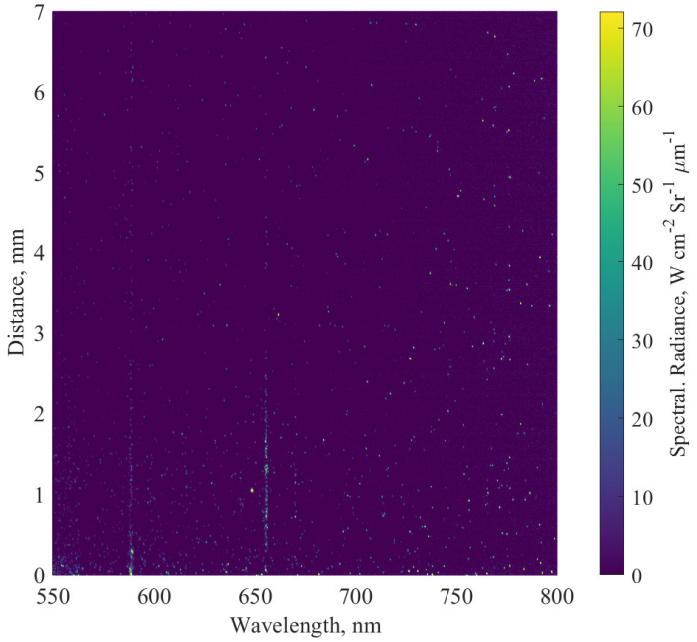

Fig. 34 Spectra obtained along the stagnation line of the sub-scale vehicle for condition A

Figure 35 shows the data spatially integrated from 0 to 2 mm with the corresponding atomic lines annotated. It is interesting that H-α is detectable in the expansion tunnel configuration, but not in the shock tube configuration. There are a number of reasons why this is the case. Firstly, the free-stream conditions were more conducive to radiation in expansion tunnel mode. The density for condition A was approximately five times higher in expansion tunnel mode than shock tube mode (6.1×10^{-5} vs 1.2×10^{-5} kg m^{-3}) and the velocity was also higher. The presence of the model allows the camera gating time to be increased in expansion tunnel mode, thus reducing the signal-to-noise ratio and potentially allowing for less intense spectral features to be resolved. The sodium line is an impurity which is relatively common in impulse facilities and could potentially be removed by employing a technique such as plasma cleaning [53].

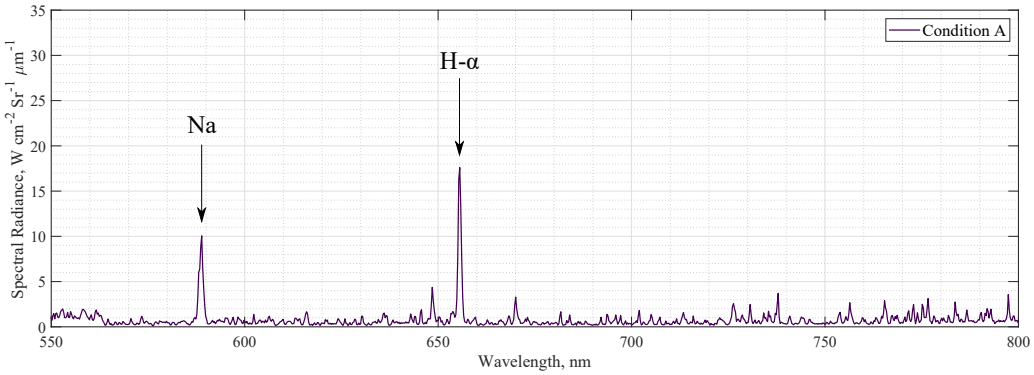

Fig. 35 Spatially integrated radiance between 0 and 2 mm

VI. Conclusion

The development and demonstration of the first Ice Giant entry simulation capability in Europe has been presented. Significant engineering upgrades have been made to the T6 Stalker Tunnel that establish it as a unique, world leading ground test facility and a key stepping stone on the path to realisation of an Ice Giant entry mission in this decade. Major upgrades include a hydrogen handling system which consists of custom explosive gas rated pipework and a dedicated, programmable logic controller safety system. The system is designed for operation with up to 100 % H_2 at test pressures that encompass peak heating points for all proposed ESA Ice Giant trajectories. A windowed steel shock tube has been designed, pressure tested, and commissioned. A contoured, Mach 10 expansion nozzle has been also designed, pressure tested, and commissioned to improve the usable core flow area. The nozzle permits testing of models up to 180 mm in diameter. These upgrades provide a new and unique shock tube and expansion tunnel ground test capability.

Experiments in shock tube mode have shown for the first time that relatively small concentrations of CH_4 could significantly change the radiative heating environment for an Ice Giant entry probe. Initial tests in expansion tunnel mode have established that the new hydrogen system and expansion nozzle are a success and that Ice Giant entry conditions could be created in T6 with a maximum speed of 18.9 $\mathrm{km\,s^{-1}}$ and test times of approximately 30 µs achieved. This level of performance is a new European wind tunnel speed record and a promising sign of the potential of T6 to contribute to Giant Planet entry research in the future. Equilibrium simulations predict that with additional upgrades T6 could simulate Saturn and low-altitude Jupiter entry conditions in expansion tunnel mode.

Funding Sources

This work is funded within an ESA initiative under contract No. 4000132571/20/NL/MG/rk.

References

[1] Collen, P., Doherty, L. J., Subiah, D., Sopek, T., Gildfind, D., Penty, R., Gollan, R., and Morgan, R., "Development and Commissioning of the T6 Stalker Tunnel," 2021, p. 41. https://doi.org/https://doi.org/10.1007/s00348-021-03298-1.

[2] Loehle, S., Fasoulas, S., Herdrich, G. H., Hermann, T. A., Massuti-Ballester, B., Meindl, A., Pagan, A. S., and Zander, F., "The Plasma Wind Tunnels at the Institute of Space Systems: Current Status and Challenges," *32nd AIAA Aerodynamic Measurement Technology and Ground Testing Conference*, American Institute of Aeronautics and Astronautics, Washington, D.C., 2016. https://doi.org/10.2514/6.2016-3201, URL https://arc.aiaa.org/doi/10.2514/6.2016-3201.

[3] Loehle, S., Meindl, A., Poloni, E., Steer, J., Sopek, T., McGilvray, M., and Walpot, L., "Experimental Simulation of Gas Giant Entry in the PWK1 Arcjet Facility including CH4," *AIAA SCITECH 2022 Forum*, American Institute of Aeronautics and Astronautics, San Diego, CA & Virtual, 2022. https://doi.org/10.2514/6.2022-0264, URL https://arc.aiaa.org/doi/10.2514/6.2022-0264.

[4] Tibère-Inglesse, A. C., McGuire, S. D., Mariotto, P., and Laux, C. O., "Validation cases for recombining nitrogen and air

plasmas," *Plasma Sources Science and Technology*, Vol. 27, No. 11, 2018, p. 115010. https://doi.org/10.1088/1361-6595/aada61, publisher: IOP Publishing.

[5] Cruden, B. A., and Bogdanoff, D. W., "Shock Radiation Tests for Saturn and Uranus Entry Probes," *Journal of Spacecraft and Rockets*, Vol. 54, No. 6, 2017, pp. 1246–1257. https://doi.org/10.2514/1.A33891, URL https://arc.aiaa.org/doi/10.2514/1.A33891.

[6] James, C. M., Gildfind, D. E., Morgan, R. G., Lewis, S. W., and McIntyre, T. J., "Experimentally Simulating Giant Planet Entry in an Expansion Tube," *Journal of Spacecraft and Rockets*, Vol. 57, No. 4, 2020, pp. 656–671. https://doi.org/10.2514/1.A34457, URL https://arc.aiaa.org/doi/10.2514/1.A34457.

[7] Stalker, R. J., "Shock tunnel measurement of ionization rates in hydrogen," *AIAA Journal*, Vol. 18, No. 4, 1980, pp. 478–480. https://doi.org/10.2514/3.7652, URL https://arc.aiaa.org/doi/10.2514/3.7652.

[8] Higdon, K. J., Cruden, B. A., Brandis, A. M., Liechty, D. S., Goldstein, D. B., and Varghese, P. L., "Direct Simulation Monte Carlo Shock Simulation of Saturn Entry Probe Conditions," *Journal of Thermophysics and Heat Transfer*, Vol. 32, No. 3, 2018, pp. 680–690. https://doi.org/10.2514/1.T5275, URL https://arc.aiaa.org/doi/10.2514/1.T5275.

[9] Inger, G. R., Higgins, C., and Morgan, R., "Generalized Nonequilibrium Binary Scaling for Shock Standoff on Hypersonic Blunt Bodies," *Journal of Thermophysics and Heat Transfer*, Vol. 17, No. 1, 2003, pp. 126–128. https://doi.org/10.2514/2.6744, URL https://arc.aiaa.org/doi/10.2514/2.6744.

[10] Stalker, R. J., "Development of a hypervelocity wind tunnel," *The Aeronautical Journal*, Vol. 76, No. 738, 1972, pp. 374–384. https://doi.org/10.1017/S000192400004327X, URL https://www.cambridge.org/core/product/identifier/S000192400004327X/type/journal_article.

[11] De Crombrugghe, G., "On binary scaling and ground-to-flight extrapolation in high-enthalpy facilities," PhD Thesis, The University of Queensland, Mar. 2017. https://doi.org/10.14264/uql.2017.456, URL http://espace.library.uq.edu.au/view/UQ:511942.

[12] Bayon, S., "CDF Study Report - Ice Giants," 2019, p. 431. URL https://sci.esa.int/s/8JgpdVA.

[13] Leibowitz, L. P., "Measurements of the structure of an ionizing shock wave in a hydrogen-helium mixture," *Physics of Fluids*, Vol. 16, No. 1, 1973, p. 59. https://doi.org/10.1063/1.1694174, URL https://aip.scitation.org/doi/10.1063/1.1694174.

[14] Leibowitz, L., "Jupiter entry simulation with the ANAA shock tube," *8th Aerodynamic Testing Conference*, American Institute of Aeronautics and Astronautics, Bethesda,MD,U.S.A., 1974. https://doi.org/10.2514/6.1974-610, URL https://arc.aiaa.org/doi/10.2514/6.1974-610.

[15] Leibowitz, L. P., and Kuo, T.-J., "Ionizational Nonequilibrium Heating During Outer Planetary Entries," *AIAA Journal*, Vol. 14, No. 9, 1976, pp. 1324–1329. https://doi.org/10.2514/3.61465, URL https://arc.aiaa.org/doi/10.2514/3.61465.

[16] Hollis, B., Wright, M., Olejniczak, J., Takashima, N., Sutton, K., and Prabhu, D., "Preliminary Convective-Radiative Heating Environments for a Neptune Aerocapture Mission," *AIAA Atmospheric Flight Mechanics Conference and Exhibit*, American Institute of Aeronautics and Astronautics, Providence, Rhode Island, 2004. https://doi.org/10.2514/6.2004-5177, URL https://arc.aiaa.org/doi/10.2514/6.2004-5177.

[17] Higgins, C. E., "Aerothermodynamics of the gas giants," 2005. URL https://espace.library.uq.edu.au/view/UQ:107366.

[18] Liu, Y., James, C. M., Morgan, R. G., and McIntyre, T. J., "Experimental validation of a test gas substitution for simulating non-equilibrium giant planet entry conditions in impulse facilities," *Experiments in Fluids*, Vol. 61, No. 9, 2020, p. 198. https://doi.org/10.1007/s00348-020-03032-3, URL http://link.springer.com/10.1007/s00348-020-03032-3.

[19] Stalker, R. J., and Edwards, B. P., "Hypersonic Blunt-Body Flows in Hydrogen-Neon Mixtures," *Journal of Spacecraft and Rockets*, Vol. 35, No. 6, 1998, pp. 729–735. https://doi.org/10.2514/2.3399, URL https://arc.aiaa.org/doi/10.2514/2.3399.

[20] Bogdanoff, D., and Park, C., "Radiative interaction between driver and driven gases in an arc-driven shock tube," *Shock Waves*, Vol. 12, No. 3, 2002, pp. 205–214. https://doi.org/10.1007/s00193-002-0157-y, URL http://link.springer.com/10.1007/s00193-002-0157-y.

[21] James, C. M., Gildfind, D. E., Lewis, S. W., Morgan, R. G., and Zander, F., "Implementation of a state-to-state analytical framework for the calculation of expansion tube flow properties," *Shock Waves*, Vol. 28, No. 2, 2018, pp. 349–377. https://doi.org/10.1007/s00193-017-0763-3, URL http://link.springer.com/10.1007/s00193-017-0763-3.

[22] Mirels, H., "Test Time in Low-Pressure Shock Tubes," *Physics of Fluids*, Vol. 6, No. 9, 1963, p. 1201. https://doi.org/10.1063/1.1706887, URL https://aip.scitation.org/doi/10.1063/1.1706887.

[23] Gildfind, D. E., James, C. M., Toniato, P., and Morgan, R. G., "Performance considerations for expansion tube operation with a shock-heated secondary driver," *Journal of Fluid Mechanics*, Vol. 777, 2015, pp. 364–407. https://doi.org/10.1017/jfm.2015.349, URL https://www.cambridge.org/core/product/identifier/S0022112015003493/type/journal_article.

[24] Collen, P., Doherty, L., and McGilvray, M., "Measurements of radiating hypervelocity air shock layers in the T6 Free-Piston Driven Shock Tube," *International conference on flight vehicles, aerothermodynamics and re-entry missions and engineering (FAR 2019)*, ESA Conference Bureau, 2019. URL https://indico.esa.int/event/272/contributions/4415/.

[25] Collen, P. L., Satchell, M., Di Mare, L., and McGilvray, M., "The influence of shock speed variation on radiation and thermochemistry experiments in shock tubes," *Journal of Fluid Mechanics*, Vol. 948, 2022, p. A51. https://doi.org/10.1017/jfm.2022.727, URL https://www.cambridge.org/core/product/identifier/S0022112022007273/type/journal_article.

[26] Michler, T., Wackermann, K., and Schweizer, F., "Review and Assessment of the Effect of Hydrogen Gas Pressure on the Embrittlement of Steels in Gaseous Hydrogen Environment," *Metals*, Vol. 11, No. 4, 2021, p. 637. https://doi.org/10.3390/met11040637, URL https://www.mdpi.com/2075-4701/11/4/637.

[27] Woods, S., and Lee, J. A., "Hydrogen embrittlement," 2016.

[28] ANSI/AIAA, "Guide to safety of hydrogen and hydrogen systems (ANSI/AIAA g-095a-2017)," , 2017.

[29] Subiah, S., Collen, P., Doherty, L., Penty Geraets, R., Hyslop, A., and McGilvray, M., "Condition development and commissioning of the Oxford T6 Stalker Tunnel in reflected shock tunnel mode," 2019. URL https://ora.ox.ac.uk/objects/uuid:706a8d91-bc67-4779-ae96-aa3be3549551.

[30] Trimpi, R. L., and Callis, L. B., *A perfect-gas analysis of the expansion tunnel: A modification to the expansion tube*, National Aeronautics and Space Administration, 1965.

[31] Callis Jr, L., "A theoretical study of the effect on expansion-tube performance of area changes at primary and secondary diaphragm stations," Tech. rep., 1966.

[32] Scott, M. P., "Development and Modelling of Expansion Tubes," Ph.D. thesis, 2006.

[33] Davey, M. G., and Litster, J., "A Hypersonic Nozzle for the X3 Expansion Tube," Ph.D. thesis, 2006.

[34] Toniato, P., Gildfind, D. E., Jacobs, P. A., and Morgan, R. G., "Expansion tube nozzle design using a parallel simplex algorithm," *Shock Waves*, Vol. 30, No. 2, 2020, pp. 185–199. https://doi.org/10.1007/s00193-019-00930-2, URL http://link.springer.com/10.1007/s00193-019-00930-2.

[35] Moses, J. I., Cavalié, T., Fletcher, L. N., and Roman, M. T., "Atmospheric chemistry on Uranus and Neptune," *Philosophical Transactions of the Royal Society A: Mathematical, Physical and Engineering Sciences*, Vol. 378, No. 2187, 2020, p. 20190477. https://doi.org/10.1098/rsta.2019.0477, URL https://royalsocietypublishing.org/doi/10.1098/rsta.2019.0477.

[36] Coelho, J. A. A., "Aerothermodynamic Analysis of Aerocapture and Ballistic Entry Flows in Neptune's Atmosphere," 2021, p. 134. https://doi.org/https://doi.org/10.1016/j.asr.2022.12.024.

[37] James, C., "Radiation from simulated atmospheric entry into the gas giants," PhD Thesis, The University of Queensland, Oct. 2018. https://doi.org/10.14264/uql.2018.697, URL http://espace.library.uq.edu.au/view/UQ:e4b2dca.

[38] Glenn, A. B., Collen, P. L., and McGilvray, M., "Experimental Non-Equilibrium Radiation Measurements for Low-Earth Orbit Return," *AIAA SCITECH 2022 Forum*, American Institute of Aeronautics and Astronautics, San Diego, CA & Virtual, 2022. https://doi.org/10.2514/6.2022-2154, URL https://arc.aiaa.org/doi/10.2514/6.2022-2154.

[39] Park, C., "Nonequilibrium air radiation (Nequair) program: User's manual," Tech. rep., 1985.

[40] Cruden, B. A., and Brandis, A. M., "Updates to the NEQAIR radiation solver," *Radiation in High Temperature Gases*, 2014. Publisher: European Space Agency St. Andrews, UK.

[41] Steer, J., Collen, P. L., Glenn, A. B., Hambidge, C., Doherty, L. J., McGilvray, M., Loehle, S., and Walpot, L., "Shock radiation tests for ice giant entry probes including CH4 in the T6 free-piston driven wind tunnel," *AIAA SCITECH 2023 forum*, 2023, p. 1729. https://doi.org/10.2514/6.2023-1729.

[42] Park, C., "Nonequilibrium Chemistry and Radiation for Neptune Entry," *Journal of Spacecraft and Rockets*, Vol. 48, No. 6, 2011, pp. 897–903. https://doi.org/10.2514/1.51810, URL https://arc.aiaa.org/doi/10.2514/1.51810.

[43] Collen, P. L., Doherty, L. J., Subiah, S. D., Hyslop, A., and McGilvray, M., "Performance Capability Experiments in T6: A Multi-Mode Ground Test Facility for High-Enthalpy, Aerothermodynamics Research," 2019, p. 8.

[44] Gibbons, N. N., Damm, K. A., Jacobs, P. A., and Gollan, R. J., "Eilmer: an Open-Source Multi-Physics Hypersonic Flow Solver," *Computer Physics Communications*, Vol. 282, 2023, p. 108551. https://doi.org/10.1016/j.cpc.2022.108551, URL http://arxiv.org/abs/2206.01386, arXiv:2206.01386 [cs].

[45] Gollan, R., and Jacobs, P., "About the formulation, verification and validation of the hypersonic flow solver Eilmer," *International Journal for Numerical Methods in Fluids*, Vol. 73, No. 1, 2013, pp. 19–57. https://doi.org/10.1002/fld.3790, URL https://onlinelibrary.wiley.com/doi/10.1002/fld.3790.

[46] Park, C., "Nonequilibrium Ionization and Radiation in Hydrogen-Helium Mixtures," *Journal of Thermophysics and Heat Transfer*, Vol. 26, No. 2, 2012, pp. 231–243. https://doi.org/10.2514/1.T3689, URL https://arc.aiaa.org/doi/10.2514/1.T3689.

[47] Milos, F. S., "Galileo Probe Heat Shield Ablation Experiment," *Journal of Spacecraft and Rockets*, Vol. 34, No. 6, 1997, pp. 705–713. https://doi.org/10.2514/2.3293, URL https://arc.aiaa.org/doi/10.2514/2.3293.

[48] Milos, F. S., Chen, Y.-K., Squire, T. H., and Brewer, R. A., "Analysis of Galileo Probe Heatshield Ablation and Temperature Data," *Journal of Spacecraft and Rockets*, Vol. 36, No. 3, 1999, pp. 298–306. https://doi.org/10.2514/2.3465, URL https://arc.aiaa.org/doi/10.2514/2.3465.

[49] Erb, A. J., West, T. K., and Johnston, C. O., "Investigation of Galileo Probe Entry Heating with Coupled Radiation and Ablation," *Journal of Spacecraft and Rockets*, Vol. 57, No. 4, 2020, pp. 692–706. https://doi.org/10.2514/1.A34751, URL https://arc.aiaa.org/doi/10.2514/1.A34751.

[50] Sutton, K., and Graves Jr, R. A., "A general stagnation-point convective heating equation for arbitrary gas mixtures," Tech. rep., 1971.

[51] Steer, J., Collen, P. L., Glenn, A. B., Sopek, T., Hambidge, C., Doherty, L. J., McGilvray, M., Loehle, S., and Walpot, L., "Experimental study of a galileo sub-scale model at ice giant entry conditions in the T6 free-piston driven wind tunnel," *AIAA SciTech 2023 forum*, 2023, p. 1339. https://doi.org/10.2514/6.2023-1339.

[52] Carroll, A. T., Brandis, A. M., and Prabhu, D. K., "Stagnation Point Convective Heating Correlations for Entry into H_2/He Atmospheres," *AIAA SCITECH 2023 Forum*, American Institute of Aeronautics and Astronautics, National Harbor, MD & Online, 2023. https://doi.org/10.2514/6.2023-0208, URL https://arc.aiaa.org/doi/10.2514/6.2023-0208.

[53] Cruden, B., Martinez, R., Grinstead, J., and Olejniczak, J., "Simultaneous Vacuum-Ultraviolet Through Near-IR Absolute Radiation Measurement with Spatiotemporal Resolution in An Electric Arc Shock Tube," *41st AIAA Thermophysics Conference*, American Institute of Aeronautics and Astronautics, San Antonio, Texas, 2009. https://doi.org/10.2514/6.2009-4240, URL https://arc.aiaa.org/doi/10.2514/6.2009-4240.